THE ASTROPHYSICAL JOURNAL, 567:980–998, 2002 March 10

METHANOL AND SILICON MONOXIDE OBSERVATIONS TOWARD BIPOLAR OUTFLOWS ASSOCIATED WITH CLASS 0 OBJECTS

GUIDO GARAY AND DIEGO MARDONES
Departamento de Astronomía, Universidad de Chile, Casilla 36-D, Santiago, Chile; guido@das.uchile.cl, mardones@das.uchile.cl
LUIS F. RODRÍGUEZ
Instituto de Astronomía, UNAM, Apartado Postal 3-72, 58089 Morelia, Michoacán, México
PAOLA CASELLI
Osservatorio Astrofisico di Arcetri, Largo Enrico Fermi 5, 50125 Firenze, Italy
AND
TYLER L. BOURKE
Harvard-Smithsonian Center for Astrophysics, 60 Garden Street, Cambridge, MA 02138
Received 2001 September 14; accepted 2001 November 13

ABSTRACT

We report Swedish-ESO Submillimetre Telescope observations of seven bipolar outflows thought to be associated with Class 0 objects in the $v = 0$ $J = 3 \rightarrow 2$ and $J = 2 \rightarrow 1$ transitions of SiO and $J_k = 3_k \rightarrow 2_k$ and $J_k = 2_k \rightarrow 1_k$ transitions of CH_3OH. Methanol and silicon monoxide emission from outflowing gas were detected toward the lobes of four objects (NGC 2264G, IRAS 16293−2422, Serpens S68N, and Serpens SMM 4). The SiO line profiles are characteristics of C-type bow shocks, showing a peak at a radial velocity close to but displaced from the ambient cloud velocity and a gradual decrease in intensity from the peak toward higher flow velocities. There is a significant correlation between the column density of SiO and the terminal SiO flow velocity, which suggests a velocity-selective enhancement in the production of SiO molecules. We find that the SiO abundance in the lobes is enhanced with respect to that of the ambient cloud by a factor of at least 330 in IRAS 16293−2422 and SMM 4, 170 in NGC 2264G, and 80 in S68N. The CH_3OH abundance is enhanced by a factor of 500 in IRAS 16293−2422, 330 in SMM 4, 80 in S68N, and 23 in NGC 2264G. In addition, we find that the dependence of the SiO/CO and CH_3OH/CO abundance ratios with radial flow velocity shows a steep increase in the range from $\sim$0 to $\sim$4–5 km s^{-1} and a gradual decline toward higher flow velocities. In the remaining three sources (CG 30, IRAS 13036−7644, and VLA 1623−243), emission in methanol was detected from a narrow line at the velocity of the ambient cloud, and no emission was detected in silicon monoxide. Weak methanol emission from a low-velocity outflow component was detected toward CG 30.

Subject headings: ISM: abundances — ISM: individual (IRAS 16293−2422, NGC 2264G, Serpens) — ISM: jets and outflows — ISM: molecules — stars: formation

1. INTRODUCTION

Theoretical calculations show that shock waves compress and heat interstellar gas and should cause substantial changes in the chemistry of the originally quiescent material. The characteristics of these effects depend on whether the shocks are of the jump (J) or continuous (C) type (see review by Draine & McKee 1993), which in turn depends on the shock velocity, magnetic field strength, and fractional ionization in the preshock gas. In high-velocity J-type shocks, with shock velocities $v_s > 50$ km s^{-1}, the temperature of the gas is high enough (10^4–10^5 K) to dissociate all molecules, which are reformed in a warm zone in the wake of the shock (Hollenbach & McKee 1989; Neufeld & Dalgarno 1989). Thermal sputtering of grain cores is expected to inject a high abundance of refractory elements such as Si and Fe. In lower speed ($v_s < 40$ km s^{-1}) C-type shocks propagating in high-density [$n(H_2) \geq 10^4$ cm^{-3}] media the temperature of the gas is increased only to $\sim 10^3$ K, and the fluid remains molecular (Draine, Roberge, & Dalgarno 1983). Several endothermic reactions proceed rapidly in the warm gas, producing species such as OH, H_2O, and H_2S, which are otherwise rare in the ambient medium. In addition, C-shocks are expected to introduce a variety of refractory and volatile species on the gas phase via nonthermal sputtering of grain cores and ice mantles (Flower & Pineau des Forêts 1995; Tielens et al. 1994; Tielens 1999).

A wealth of observations have shown that bipolar molecular outflows are a common phenomena in the process of star formation (see reviews by Bachiller 1996; Bachiller & Tafalla 1999; Richer et al. 2000). During their earliest phase of evolution, stellar objects generate a fast, well-collimated bipolar wind, which is thought to drive away the original angular momentum of the collapsing cloud core. As the high-velocity gas interacts with and sweeps up the surrounding ambient gas and dust, shock waves are driven into the quiescent ambient medium, giving rise to the molecular outflows. Outflows from young stars are then expected not only to affect considerably the physical properties of the surrounding gas but to produce significant alterations in the chemistry of the ambient medium. They create high-temperature shocks and lower temperature turbulent regions in which the icy mantles and refractory material can be returned to the gas phase. Thus, studies of the chemical

TABLE 1

OBSERVATIONAL PARAMETERS

Molecule	Transition	Frequency (MHz)	Beam Size (FWHM) (arcsec)	η	Δv (km s^{-1})
CH_3OH.....	$J_k = 2_0 \rightarrow 1_0\ A^+$	96741.42	52	0.73	0.130
	$J_k = 3_{-1} \rightarrow 2_{-1}\ E$	145097.470	34	0.66	0.086
SiO	$v = 0$ J = 2 → 1	86846.998	57	0.75	0.144
	$v = 0$ J = 3 → 2	130268.702	40	0.68	0.096
CS	J = 2 → 1	97980.968	52	0.73	0.132
	J = 3 → 2	146969.049	34	0.66	0.088
CO	J = 1 → 0	115271.204	45	0.70	0.109
	J = 2 → 1	230537.990	23	0.60	0.054
^{13}CO	J = 1 → 0	110201.353	45	0.70	0.114
	J = 2 → 1	220398.686	23	0.60	0.057

composition of bipolar molecular outflows allows for the investigation of their structure. In addition, since shocks are transient phenomena, it should be possible to use molecules with enhanced abundances as temporal indicators and hence as signposts of the evolutionary state of the outflow.

Whereas a substantial amount of work has been devoted to the determination of the physical characteristics of outflows, very little is known about their chemical properties. Few multiline mappings of molecular outflows have been performed to date (Blake et al. 1995; Bachiller & Pérez Gutiérrez 1997; Garay et al. 1998; Bachiller et al. 2001). In this article we report molecular observations of seven collimated outflows associated with Class 0 objects in rotational transitions of silicon monoxide (SiO) and methanol (CH_3OH). These highly collimated outflows are thought to be driven by jets that accelerate the ambient gas through the propagation of shocks (e.g., Raga & Cabrit 1993). The main goals of these observations are to determine how the chemistry of ambient molecular material is affected by the interaction with high-velocity jets from young stellar objects, to investigate whether or not the strength of the emission in these molecules is correlated with the velocity of the flow and/or with physical parameters of the ambient cloud, and to assess whether or not the abundance of these molecular species serves as a sensitive probe of the evolutionary stage of bipolar outflows (e.g., van Dishoeck & Blake 1998).

2. OBSERVATIONS

The observations were carried out using the 15 m Swedish-ESO Submillimetre Telescope (SEST) located on La Silla, Chile, during 1997 March and September, 1998 January, and 1999 February. The molecules, transitions, and frequencies observed and the instrumental parameters are summarized in Table 1. We used the 150 and 100 GHz SiS receivers to simultaneously observe 2 and 3 mm lines of silicon monoxide, methanol, and carbon monosulfide. Single-sideband receiver temperatures were typically 120 K for both receivers. As back end, we used high-resolution acousto-optical spectrometers providing a channel separation of 43 kHz and a total bandwidth of 43 MHz. The bandwidth chosen for the methanol observations at 2 mm wavelengths contains three rotational lines of CH_3OH (the $3_0 \rightarrow 2_0\ E$, $3_{-1} \rightarrow 2_{-1}\ E$, and $3_0 \rightarrow 2_0\ A^+$ transitions at rest frequencies of 145,093.75, 145,097.47, and 145,103.23 MHz) and the $3_{12} \rightarrow 2_{21}$ rotational line of C_3H_2 (rest frequency of 145,089.636 MHz). The bandwidth at 3 mm wavelengths contains three lines of CH_3OH (the $2_{-1} \rightarrow 1_{-1}\ E$, $2_0 \rightarrow 1_0\ A^+$, and $2_0 \rightarrow 1_0\ E$ transitions at rest frequencies of 96,739.39, 96,741.42, and 96,744.58 MHz).

The SiO and CH_3OH emissions were mapped toward the seven bipolar outflows listed in Table 2, within regions encompassing the CO lobes and centered on the *IRAS* positions (given in cols. [2] and [3]). The angular spacing was

TABLE 2

OBSERVED BIPOLAR OUTFLOWS

			SiO $v = 0$				CH_3OH			
			$J = 2 \rightarrow 1$		$J = 3 \rightarrow 2$		$J = 2 \rightarrow 1$		$J = 3 \rightarrow 2$	
SOURCE (1)	α(1950.0) (2)	δ(1950.0) (3)	t_{in} (minutes) (4)	σ[a] (mK) (5)	t_{in} (minutes) (6)	σ (mK) (7)	t_{in} (minutes) (8)	σ (mK) (9)	t_{in} (minutes) (10)	σ (mK) (11)
NGC 2264G	06 38 25.8	09 58 52.0	10	33	...	...	...	...	10	51
IRAS 08076−3556.....	08 07 40.2	−35 56 07.0	7	33[b]	6	50[b]	6	48	7	55
IRAS 13036−7644.....	13 03 41.4	−76 44 03.0	10	30	8	49	4	57	7	53
VLA 1623−243	16 23 24.9	−24 17 46.0	4	51	...	...	...	...	4	75
IRAS 16293−2422.....	16 29 20.9	−24 22 16.0	6	50	...	...	...	...	6	123
S68N	18 27 15.2	01 14 47.0	9	41	6	62	...	...	6	75
SMM 4.....	18 27 24.3	01 11 11.0	5	49	7	47	4	52	5	69

NOTE.—Units of right ascension are hours, minutes, and seconds, and units of declination are degrees, arcminutes, and arcseconds.

[a] The 1 σ rms noise in antenna temperature.

[b] For Hanning smoothed spectra.

30″ for all sources except NGC 2264G, for which we used a 40″ spacing. Columns (4)–(11) of Table 2 give the integration times on source per position and the resulting rms noise in antenna temperature (T_A^*) in each of the observed transitions. In addition we mapped, with an angular spacing of 30″, the CS emission from object CG 30.

Observations of the CO and ^{13}CO emission were made toward selected positions within each source, usually at the peak of the integrated emission in the methanol and silicon monoxide lines. The $J = 2 \rightarrow 1$ and $1 \rightarrow 0$ lines of CO and ^{13}CO were observed simultaneously using the 230 and 115 GHz SiS receivers. Single-sideband receiver temperatures were typically 150 K for both receivers. These observations were performed in the position-switching mode, with an OFF position that was previously checked to be free of emission. The integration times on source per position were 4 minutes for CO and 15–30 minutes for ^{13}CO. The goal of these observations was to obtain sensitive data in order to determine CO column densities over a wide range of flow velocities, which in turn will allow the derivation of abundance enhancements relative to CO.

3. RESULTS

In this section we present the observational results for each outflow individually. In each subsection we first give a short description of the observed properties of the CO outflows and of their driving energy source. The radial flow velocity, $v_{\rm flow}$, is defined as $v_{\rm LSR} - v_0$, where v_0 is the systemic velocity of the ambient gas.

3.1. *NGC 2264G*

The NGC 2264G molecular outflow, discovered by Margulis & Lada (1986), is located in the Monoceros OB1 molecular cloud at the distance of 800 pc (Walker 1956). It exhibits a highly collimated bipolar morphology (Margulis, Lada, & Snell 1988; Margulis et al. 1990) and a remarkable Hubble law velocity field with the outflow velocity increasing linearly with distance from the central source (Lada & Fich 1996). The collimation of the flow increases systematically with flow velocity and distance from the driving source; the opening angle is 5° for the highest velocity emission (24.5 kms^{-1} $< |v_{\rm flow}| <$ 34.5 km s^{-1}) and 25° for the lowest velocity emission (1.5 kms^{-1} $< |v_{\rm flow}| <$ 3.5 km s^{-1}). The ambient cloud velocity is assumed to be 4.6 km s^{-1} (Lada & Fich 1996). These characteristics suggest that the high-velocity gas is driven by a jet, whereas the low-velocity gas corresponds to swept-up ambient gas. The energy source (IRAS 06384+0958) has been identified at centimeter wavelengths with the VLA by Gómez et al. (1994) and confirmed as a Class 0 type object at submillimeter wavelengths by Ward-Thompson, Eiroa, & Casali (1995), who derived a bolometric luminosity of $\sim$12 $L_\odot$.

The observed spectra in the SiO ($2 \rightarrow 1$) and CH_3OH ($3_k \rightarrow 2_k$) lines are presented in Figure 1. Emission is detected only toward the west (blueshifted) lobe of the CO outflow. Neither methanol nor silicon monoxide were detected toward the east (redshifted) lobe. The range of radial flow velocity observed in SiO and CH_3OH is significantly smaller than that of the CO emission, which exhibits emission up to a radial flow velocity of the order of -40 km s^{-1}. This is illustrated in Figure 2, which shows position-velocity (p-v) diagrams for SiO and CH_3OH along the CO outflow axis (P.A. of 101°). The radial flow velocity extends up to -6.8 km s^{-1} in SiO and -6.0 km s^{-1} in CH_3OH. The SiO line profiles show a peak at a radial velocity close to the ambient cloud velocity, a gradual decrease in intensity toward blueshifted velocities, and a rapid decline toward the ambient cloud velocity, suggesting that a small fraction of the molecular gas is accelerated to shock velocities while the majority remains close to the ambient cloud velocity. This type of profile is characteristic of C-type bow shocks, where a range of shock speeds is present (Smith & Brand 1990).

Figure 3 shows contour maps of the velocity-integrated SiO and CH_3OH wing emission in the range of radial flow velocities from -7.2 to -1.0 km s^{-1} (*continuous lines*; blueshifted gas) and from 1.0 to 7.2 km s^{-1} (*dotted lines*; redshifted gas). The spatial distribution of the CH_3OH and SiO emission from the west lobe is similar to that of the poorly collimated CO emission from the low-velocity blueshifted outflowing gas (-3.6 km s^{-1} $< v_{\rm flow} < -1.6$ km s^{-1}; see Fig. 3 of Lada & Fich 1996). Further, the peak of the emission is closely associated with bright shock-excited knots of H_2 emission (Davis & Eislöffel 1995; Fich & Lada 1997). These characteristics and those of the line profiles suggest that the SiO and CH_3OH emission from the blue lobe arises in low-velocity shocks, possibly in the wake behind a bow shock, and that the underlying wind is a wide-angle wind. The origin of the asymmetry in the emission from the east and west lobes is not clear, although it can be ascribed to differences in the physical environment into which the bipolar flow is propagating (Lada & Fich 1996). The blue lobe is interacting strongly with the ambient medium, as shown by the presence of the H_2 emission at the peak of the CH_3OH and SiO emission. No such H_2 emission is observed in the red lobe. Lada & Fich (1996) show that a clump of ambient gas is also located at this position, and a highly collimated high-velocity CO jet originates there. No such structures are present in the red lobe.

3.2. *IRAS 08076−3556 (CG 30)*

CG 30 (DC 253.3−1.6, Hartley et al. 1986; BHR 12, Bourke, Hyland, & Robinson 1995a) is a small cometary globule, $\sim$2′ in diameter, within the OB association Pup OB3 (Westerlund 1963). Near the center of the globule lies the source IRAS 08076−3556, which has a luminosity of 12.8 $L_\odot$ for a distance of 400 pc (Persi et al. 1990) and a bolometric temperature of 74 ± 15 K (Gregersen et al. 1997), which puts it on the boundary of the Class 0 category (Chen et al. 1995). The globule is associated with several signposts of shock and outflow activity, such as a low-excitation Herbig-Haro object (HH 120; Reipurth 1981; Pettersson 1984), H_2 emission (Gredel 1994), and an east-west molecular outflow that does not show well-collimated lobes (Olberg, Reipurth, & Booth 1989). Hoddap & Ladd (1995) detected in the $S(1)$ line of molecular hydrogen several emission knots that morphologically appear as a well-collimated bipolar jet aligned roughly in a northeast-southwest direction. The HH object is elongated in a different direction than that of the H_2 jet, suggesting that they may be powered by different sources. HH 120 is most likely associated with CG 30–IRS 4 (Pettersson 1984; Zinnecker et al. 1999), which is also thought to be the driving source of the molecular outflow. The driving source of the H_2 jet, undetected at near-infrared wavelengths (Hodapp & Ladd 1995; Zinnecker et al. 1999), has been recently detected at submillimeter wavelengths with SCUBA (Henning et al. 2001) and lies $\sim$20″ south of IRS 4.

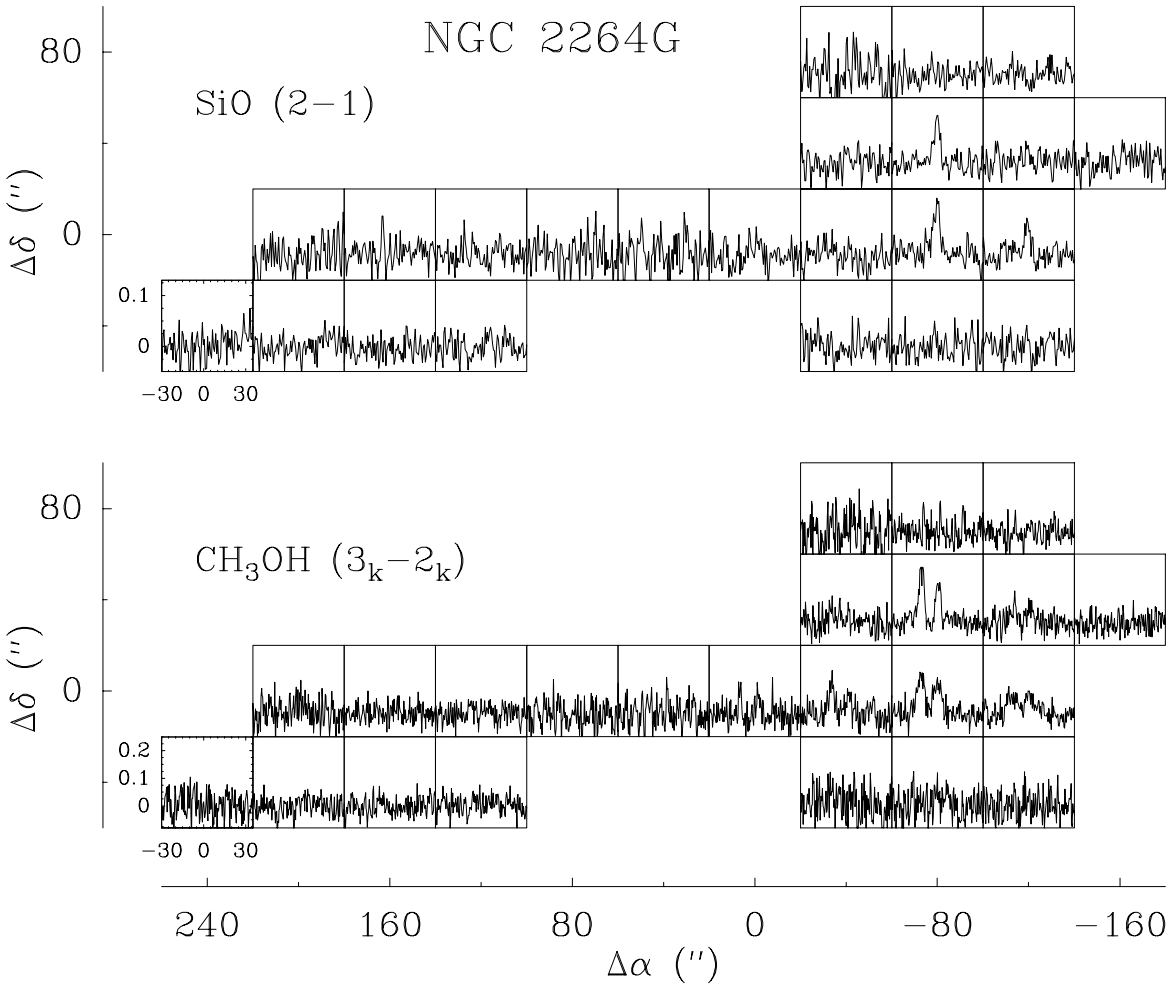

FIG. 1.—Observed spectra of the SiO ($2 \rightarrow 1$) (*top*) and CH_3OH ($3_k \rightarrow 2_k$) (*bottom*) line emissions toward the NGC 2264G outflow. The grid spacing is 40″. Offsets are from the reference position at $\alpha = 06^h38^m25^s.80$ and $\delta = 9°58'52''$ (B1950.0), which is the position of the driving source VLA 2 (Gómez et al. 1994). In each box the velocity scale ranges from -30 to 35 km s^{-1}. The antenna temperature scale is from -0.05 to 0.13 K for SiO ($2 \rightarrow 1$) and -0.08 to 0.25 K for CH_3OH ($3_k \rightarrow 2_k$).

Toward CG 30 we mapped, in addition to SiO and CH_3OH, the emission in the $J = 3 \rightarrow 2$ and $J = 2 \rightarrow 1$ lines of CS. The observed spectra in CS and CH_3OH are shown in Figure 4. No emission was detected in SiO ($T_A < 0.05$ K) within the mapped region. In the methanol spectra at 145 GHz also detected is emission in the 3_{12}–2_{21} line of C_3H_2. The carbon monosulfide and methanol line profiles show emission from a strong and narrow ($\Delta v \sim 1.0$ km s^{-1}) component with a central velocity of 6.26 ± 0.4 km s^{-1}, similar to the velocity of the dense globule measured in ammonia lines of 6.15 km s^{-1} (Persi et al. 1994; Bourke et al. 1995b). The spatial distribution of the ambient cloud emission in lines of CS and CH_3OH is presented in the left panels of Figure 5. The narrow CS line emission arises from a region of $\sim 86''$ in diameter (FWHM), which is similar in extent to that of the cometary globule as seen in optical images (e.g., Pettersson 1984) but smaller than the NH_3 core ($140'' \times 100''$) mapped with a larger beam (Bourke et al. 1995b). The CS and CH_3OH spectra also show weak emission from a pedestal component, covering the range of flow velocities from -3.4 km to 3.8 km s^{-1}. The spatial distribution of the wing emission is presented in the right panels of Figure 5. Redshifted emission is detected toward the eastern region of the globule, both in CS and CH_3OH, whereas blueshifted emission is detected toward the central region and only in CS. The presence of outflowing gas is also indicated by the lines profiles of the CO emission observed at the central position, which show redshifted and blueshifted emissions up to radial flow velocities of $\sim +12$ and ~ -10 km s^{-1}, respectively.

3.3. *IRAS 13036−7644 (DC 303.8−14.2)*

The Bok globule DC 303.8−14.2 (Hartley et al. 1986; BHR 86, Bourke et al. 1995a) is located in the eastern part of the Chamaeleon II dark cloud complex, at a distance of 200 pc (Whittet et al. 1991; Hughes & Hartigan 1992). It is associated with the *IRAS* source 13036−7644, which has a luminosity of 0.47 $L_\odot$ and a bolometric temperature of 63 K (Chen et al. 1997). Molecular line observations toward the *IRAS* source show double-peaked profiles, which are ambiguous regarding the kinematics of the gas. The CS ($2 \rightarrow 1$) and H_2CO ($2_{12} \rightarrow 1_{11}$) lines show a brighter blueshifted component, characteristic of infalling motions (Mardones et al. 1997). On the other hand, the CO ($1 \rightarrow 0$), CO ($2 \rightarrow 1$), and HCO^+ ($1 \rightarrow 0$) profiles show a stronger redshifted peak, characteristic of expansion motions (Lehtinen 1997). Lehtinen (1997) reported a low-velocity molecular outflow ($|v_{\rm flow}| \leq 4$ km s^{-1}) oriented approx-

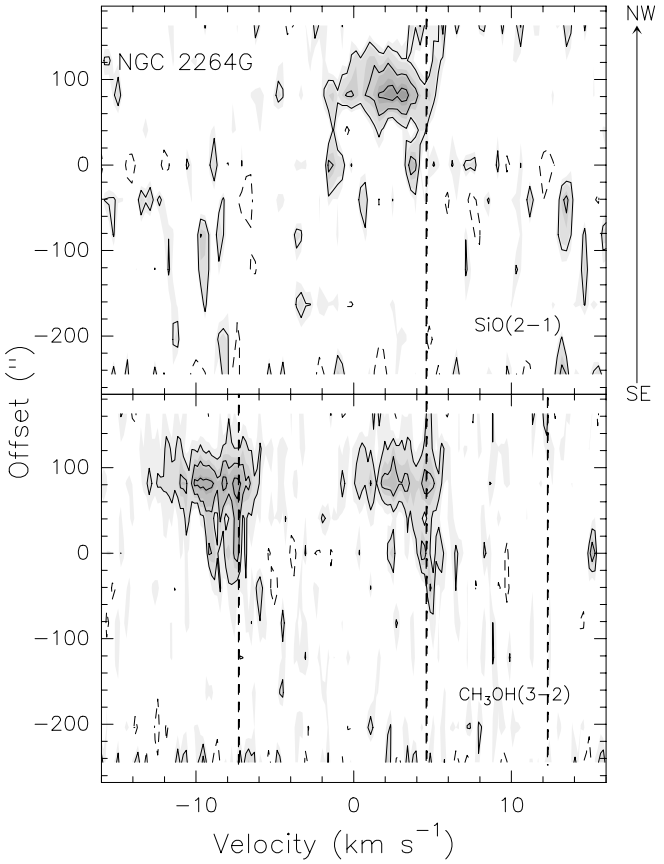

FIG. 2.—Position-velocity diagrams along the symmetry axis of the NGC 2264G outflow (P.A. 101°). *Top*: SiO ($2 \rightarrow 1$) emission. Contour levels are drawn at -0.03 K and from 0.03 to 0.12 K in steps of 0.03 K. The vertical dotted line indicates the systemic velocity of the ambient gas of 4.6 km s^{-1}. *Bottom*: CH_3OH ($3_k \rightarrow 2_k$) emission. Contour levels are drawn at -0.05 K and from 0.05 to 0.25 K in steps of 0.05 K. The vertical dotted lines indicate the position of the different k-components for a systemic velocity of 4.6 km s^{-1}.

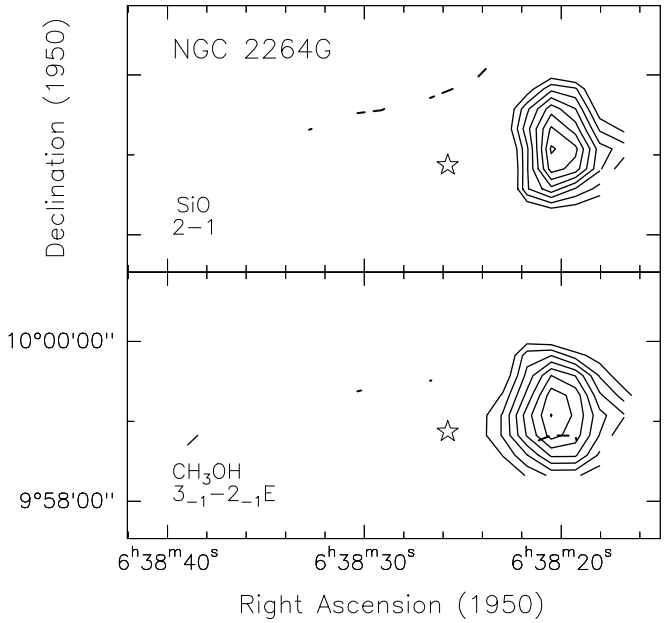

FIG. 3.—Contour maps of velocity-integrated line wing emission from the NGC 2264G bipolar outflow. Continuous lines represent blueshifted emission ($v_{\rm flow}$: -7.2 to -1.0 km s^{-1}), dashed lines redshifted emission ($v_{\rm flow}$: 1.0 to 7.2 km s^{-1}), and the star marks the position of the radio continuum source VLA 2 (Gómez et al. 1994). *Top*: SiO ($2 \rightarrow 1$) emission. Lowest contour and contour interval are 0.15 and 0.05 K km s^{-1}. *Bottom*: CH_3OH ($3_{-1} \rightarrow 2_{-1}$ *E*) emission. Lowest contour and contour interval are 0.18 and 0.06 K km s^{-1}.

imately in the east-west direction, which is thought to be driven by IRAS 13036−7644. From *ISO* observations, Lehtinen, Lemke, & Mattila (1999) suggest that this source is a transitional object between Class 0 and Class I.

The observed spectra in methanol are shown in Figure 6. No emission was detected in SiO ($T_A < 0.05$ K) within the mapped region. The methanol profiles show emission from a narrow component with an average center velocity of 3.82 ± 0.01 km s^{-1} and an average line width of $\sim$0.7 km s^{-1}. Also detected is emission in the 3_{12}–2_{21} line of C_3H_2. Maps of the velocity integrated emission in the CH_3OH (3_0–2_0 A^+) and C_3H_2 (3_{12}–2_{21}) lines are shown in Figure 7. The methanol emission arises from a region of $93'' \times 72''$ in size (FWHM), which is significantly smaller than that of the dark globule of $14' \times 6'$ (Hartley et al. 1986) and marginally smaller than the ammonia core ($144'' \times 84''$) mapped with a larger beam (Bourke et al. 1995b). We find that the line widths of the methanol emission toward the center of the globule are different in the different transitions, increasing with the energy of the upper level of the transition from $\sim$0.7 km s^{-1} at the lower energies to $\sim$1.4 km s^{-1} at the higher energies. This trend suggests the presence of a spatially unresolved component of warm gas, possibly excited by the central source, whose emission blended with that of the ambient gas produces the observed line widths.

3.4. *VLA 1623−243*

This highly collimated and extended ($>10'$) outflow (André et al. 1990; Dent, Matthews, & Walther 1995) is located in the L1686 core of the ρ Ophiuchi molecular cloud complex, at a distance of 125 pc (see Wilking & Lada 1983). It shows CO wings extending up to radial outflow velocities of $\sim$25 km s^{-1} and has a dynamical timescale of $\sim 2 \times 10^3$ yr (André et al. 1990), making it one of the youngest known outflows. The driving source has been identified with the radio continuum source VLA 1623−243 (André et al. 1990; Leous et al. 1991) and has a luminosity of $\sim 0.6\, L_\odot$ (André, Ward-Thompson, & Barsony 1993). André et al. (1993) proposed VLA 1623−243 as the prototype of a new class of extremely young collapsing objects, referred to as Class 0, for which the mass in the collapsing circumstellar envelope is greater than that of the central protostar.

The observed spectra in the CH_3OH ($3_k \rightarrow 2_k$) and SiO ($2 \rightarrow 1$) lines are shown in Figure 8. Methanol emission was detected in all the observed positions, whereas weak SiO emission was detected toward the north of VLA 1623−243 but not along the symmetry axis of the CO outflow. Cyclopropenylidene (C_3H_2) emission was also detected north of VLA 1623−243. The line profiles of the methanol and silicon monoxide emission are narrow, with typical line widths of $\Delta v \sim 1.6$ km s^{-1}. Figure 9 presents a p-v diagram of the CH_3OH emission along the symmetry axis of the CO outflow (P.A. of 120°), showing that emission is detected across the whole extent of the CO lobes and in a narrow velocity range. We conclude that the methanol emission observed toward the CO lobes arises from ambient gas, no emission being detected from the outflow component.

Figure 10 shows contour maps of the velocity-integrated emission in lines of methanol and silicon monoxide. The

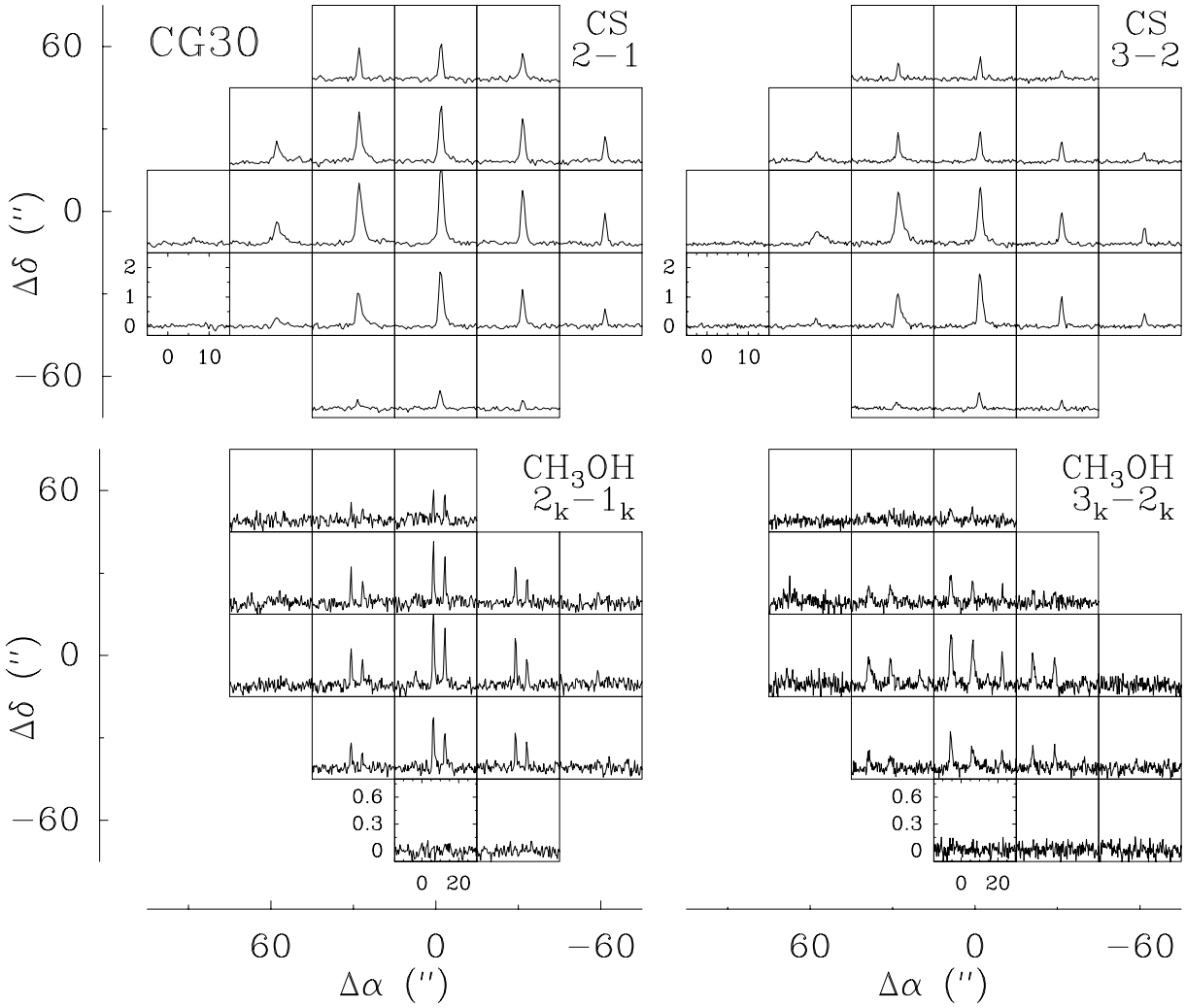

FIG. 4.—Observed spectra of the CS and CH_3OH line emission toward the CG 30 outflow. The grid spacing is 30″. Offsets are from the *IRAS* position at $\alpha = 08^h07^m40\overset{s}{.}20$ and $\delta = -35°56'07''$ (B1950.0). For the CS lines the velocity scale ranges from -5 to 15 km s^{-1} and the antenna temperature scales from -0.3 to 2.5 K. For the CH_3OH lines the velocity scale ranges from -15 to 30 km s^{-1} and the antenna temperature from -0.12 to 0.80 K.

position of the peak methanol emission lies at the edge of the northwest lobe of the CO outflow emission and is close to the position of the peak DCO^+ emission associated with the ρ Oph A core (Loren & Wootten 1986). No dust continuum source is detected toward the methanol peak. The CO $(1 \rightarrow 0)$ spectra observed toward this position shows a double-peaked line profile, with a strong blueshifted peak at the velocity of 2.3 km s^{-1} and a weaker redshifted peak at a velocity of 5.0 km s^{-1}, whereas the ^{13}CO $(1 \rightarrow 0)$ line profile shows a single component with a line center velocity of 3.18 km s^{-1}.

3.5. *IRAS 16293−2422*

IRAS 16293−2422 (hereafter IRAS 16293) is a cold infrared source, located in the ρ Ophiuchi cloud complex, with a bolometric luminosity of 23 $L_\odot$ (Walker et al. 1986). Interferometric radio continuum observations show the presence of two objects with a separation of $\sim 5''$ (Wootten 1989), suggesting that IRAS 16293 harbors a young protobinary system. The stronger radio source (IRAS 16293−2422A) has a spectral index of 0.6 ± 0.1 (Estalella et al. 1991), characteristic of stellar wind sources. The radio sources are associated with two unresolved (angular sizes less than 1″.5) millimeter dust continuum sources (Walker, Carlstrom, & Bieging 1993) that are surrounded by a circumbinary envelope of size 10″–20″, which is in turn embedded in a cold molecular core (Menten et al. 1987; Mundy, Blake, & Sargent 1992). The kinematics of the molecular gas in IRAS 16293 have been the subject of considerable debate. Whereas Walker et al. (1986) suggested that gas is in the process of collapse, Menten et al. (1987) concluded that the observed line asymmetries were due to rotation. More recently, the line profiles have been modeled as arising from infall with rotation (Zhou 1995; Narayanan, Walker, & Buckley 1998). An unusual molecular outflow, possessing four separate lobes, is observed toward IRAS 16293 (Fukui et al. 1986; Walker et al. 1988; Mizuno et al. 1990). The quadrupolar structure suggests that there are two separate bipolar outflows, one of them possibly emanating from IRAS 16293A (Walker et al. 1988; Walker, Carlstrom, & Bieging 1993; Narayanan et al. 1998). We assume an ambient cloud velocity of 3.8 km s^{-1} (see Castets et al. 2001), which corresponds to the average central velocity of the ammonia emission across the region (Mizuno et al. 1990).

The observed spectra in the SiO $(2 \rightarrow 1)$ and CH_3OH $(3_k \rightarrow 2_k)$ lines are shown in Figure 11. Strong emission in

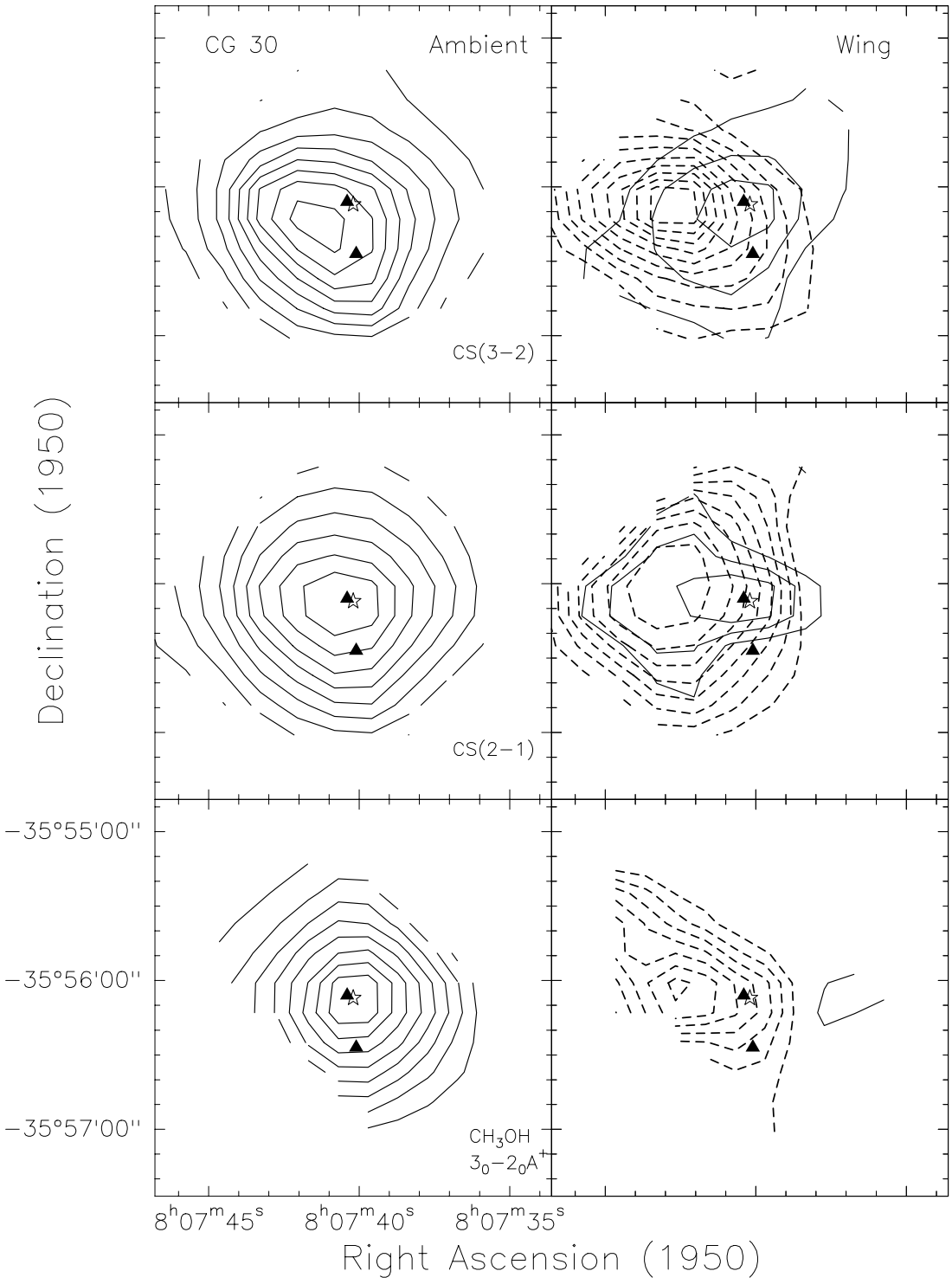

FIG. 5.—Contour maps of velocity-integrated emission from the CG 30 globule. The star marks the position of IRAS 08076−3556 and the triangles those of the submillimeter sources (Henning et al. 2001). *Left panels*: Ambient gas emission. The range of integration in v_{LSR} is from 5.26 to 7.26 km s^{-1}. Contour levels are drawn at 10%, 20%, 30%, 40%, 50%, 60%, 70%, 80%, and 90% of the peak integrated intensity of 2.8 K km s^{-1} for CS ($3 \rightarrow 2$) (*top*), 3.3 K km s^{-1} for CS ($2 \rightarrow 1$) (*middle*), and 0.90 K km s^{-1} for CH_3OH ($3_0 \rightarrow 2_0\, A^+$) (*bottom*). *Right panels*: Outflowing gas emission. Continuous lines represent blueshifted emission (v_{flow}: −3.5 to −1.3 km s^{-1}) and dashed lines redshifted emission (v_{flow}: 1.6 to 3.7 km s^{-1}). Lowest contour and contour interval are both 0.07 K km s^{-1} for CS ($3 \rightarrow 2$), 0.10 and 0.05 K km s^{-1} for CS ($2 \rightarrow 1$), and 0.06 and 0.03 K km s^{-1} for CH_3OH ($3_0 \rightarrow 2_0\, A^+$).

silicon monoxide and methanol is detected from the outflowing gas. In SiO, the higher redshifted velocities are found toward the northeast [position (90″, 60″); $v_{flow} \sim 14.2$ km s^{-1}]. The most blueshifted velocities in SiO are found at positions (90″, −60″) ($v_{flow} \sim -3.3$ km s^{-1}) and (60″, +30″) ($v_{flow} \sim -4.2$ km s^{-1}). Note that in the last position also detected is strong redshifted emission. The spatial distribution of the velocity-integrated SiO $J = 2 \rightarrow 1$ emission is shown in gray scale in the upper panel of Figure 12. The overall morphology is in good agreement with that recently presented by Hirano et al. (2001) and by Castets et al. (2001), with the bulk of the integrated emission arising from

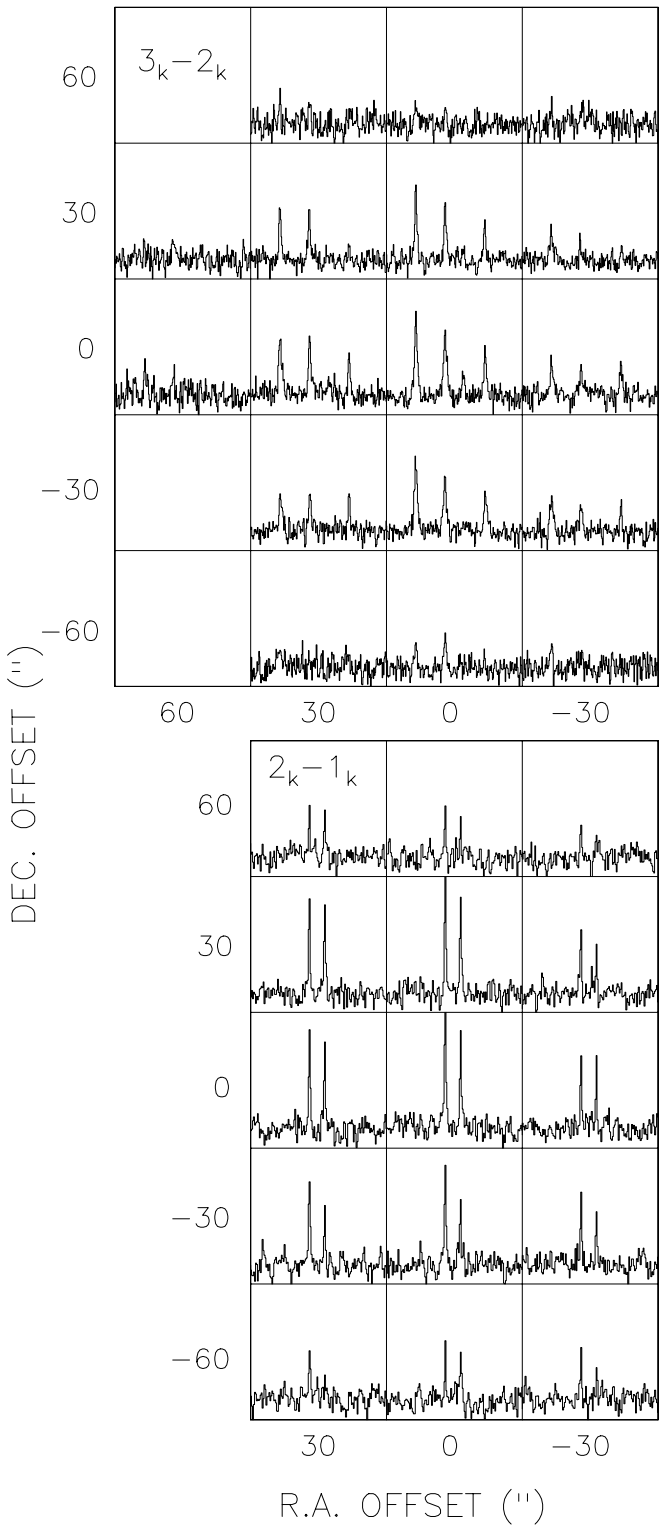

FIG. 6.—Observed spectra of the CH_3OH line emission toward the IRAS 13036−7644 outflow. The grid spacing is 30″. Offsets are from the *IRAS* position at $\alpha = 13^h03^m41^s.40$ and $\delta = -76°44'03''$ (B1950.0). In each box the velocity scale ranges from −20 to 35 km s^{-1} and the antenna temperature scale ranges from −0.12 to 0.75 K.

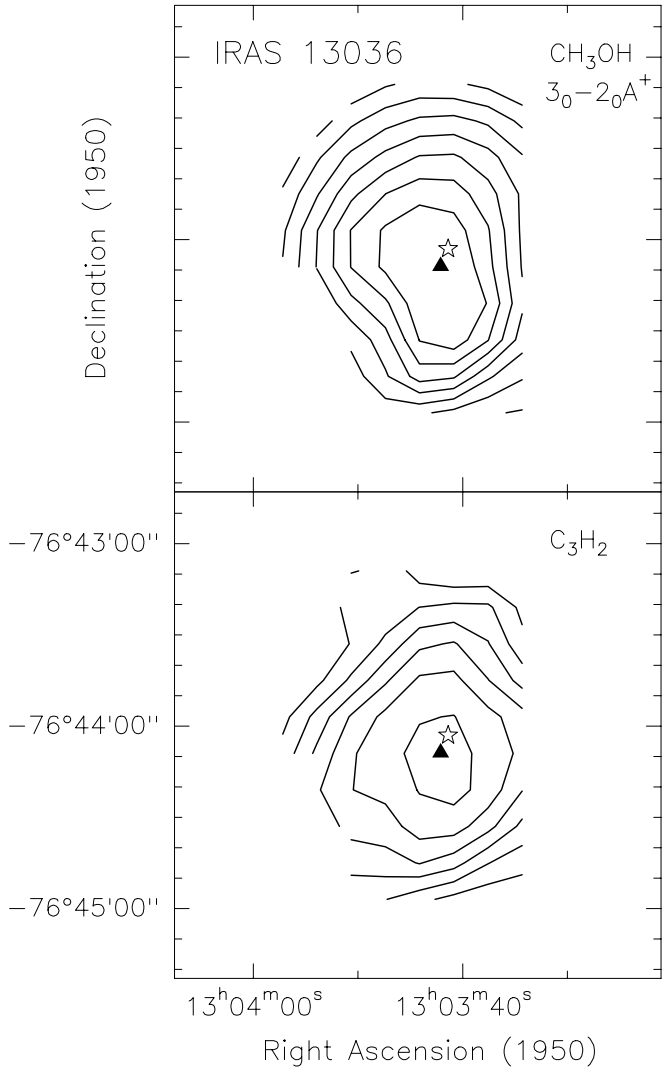

FIG. 7.—Contour maps of velocity-integrated emission from IRAS 13036−7644. The star marks the position of the *IRAS* source and the triangle the position of the radio source detected by Lehtinen (1998). *Top panel*: CH_3OH ($3_0 \rightarrow 2_0$ A^+) emission. Contour levels are drawn at −20%, 20%, 30%, 40%, 50%, 60%, 70%, 80%, and 90% of the peak integrated intensity of 0.75 K km s^{-1}. *Bottom panel*: C_3H_2 ($3_{12} \rightarrow 2_{21}$) emission. Contour levels are drawn at −20%, 20%, 35%, 50%, 65%, 80%, and 95% of the peak integrated intensity of 0.40 K km s^{-1}.

the northern region of the map. We do, however, detect weak emission from the southeast region of the map, which is not detected by Hirano et al. (2001) or Castets et al. (2001) because of their lower sensitivity.

The spatial distribution of the red and blue wing emission in SiO and CH_3OH lines is presented in Figure 12. The range of integration in flow velocity for the blueshifted and redshifted emission are, respectively, −6.4 to −1.1 and 2.9 to 14.3 km s^{-1} for silicon monoxide, and −5.1 to −1.3 and 1.5 to 6.5 km s^{-1} for methanol. The redshifted range for the CH_3OH (3_0–2_0 A^+) emission was chosen to avoid overlap with blueshifted emission from the CH_3OH (3_{-1}–2_{-1} E) line. Redshifted emission is seen mainly toward the north and blueshifted emission mainly toward the south. In addition, the wing emission from the east is considerably stronger than from the west. The overall morphology of the SiO and CH_3OH wing emission shows a quadrupolar appearance, similar to that of the CO wing emission (Walker et al. 1988; Mizuno et al. 1990). There are, however, distinct differences in the peak position and in the relative strength of the emission in the different molecules. For instance, in SiO and CH_3OH the strongest integrated wing emission is

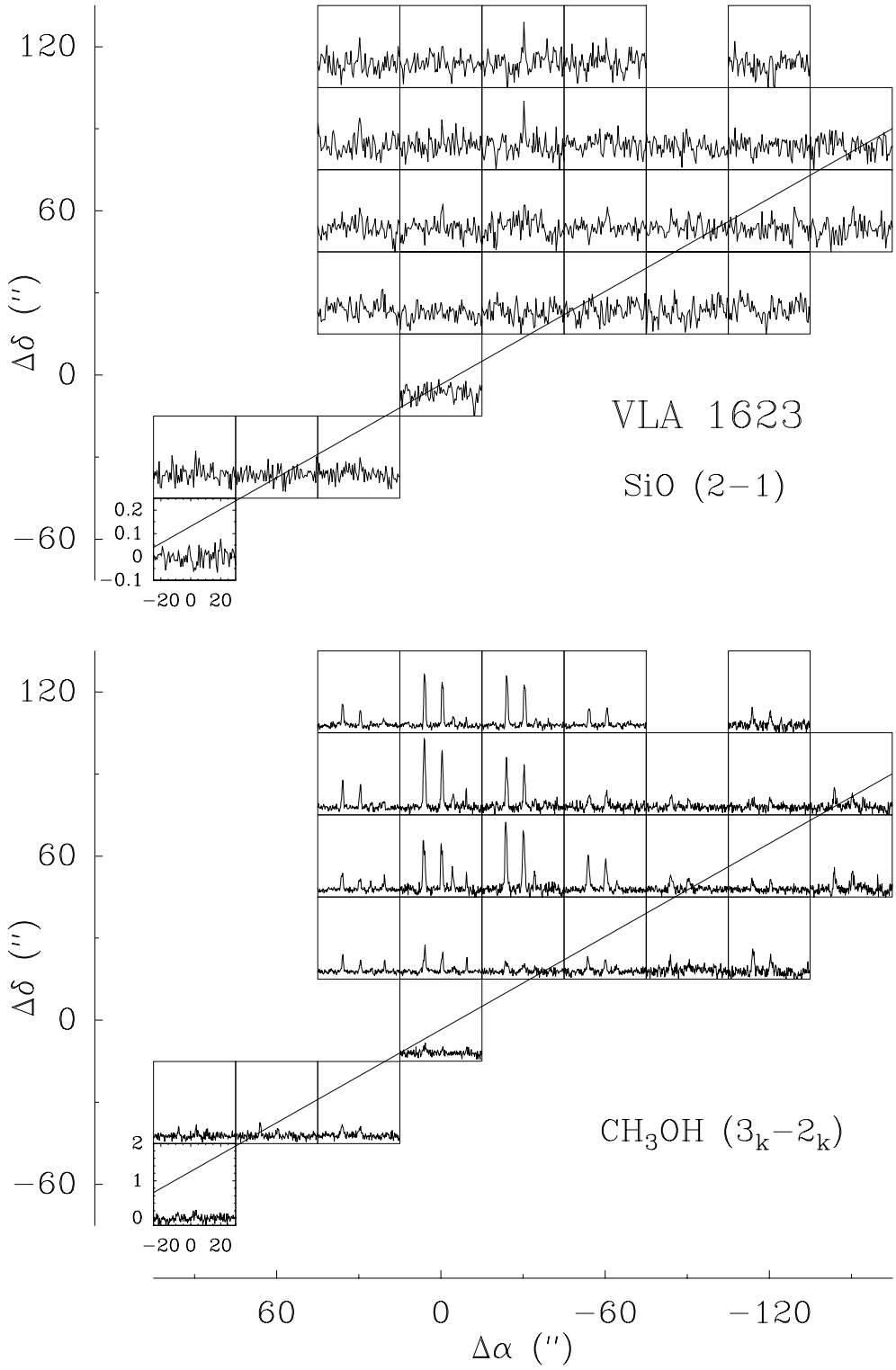

FIG. 8.—Observed spectra of the SiO ($2 \rightarrow 1$) (*top*) and CH_3OH ($3_k \rightarrow 2_k$) (*bottom*) line emission toward VLA 1623. The grid spacing is 30″. Offsets are from the reference position at $\alpha = 16^h23^m24^s.90$ and $\delta = -24°17'46''$ (B1950.0). In each box the velocity scale ranges from −25 to 30 km s^{-1}. The antenna temperature scale is from −0.2 to 2.0 K for CH_3OH and from −0.10 to 0.25 K for SiO. The line indicates the symmetry axis of the CO outflow.

found toward the northeast region of the map, whereas in CO it is toward the west of the central energy sources (Walker et al. 1988). In the following discussion we use for comparison the map of the CO outflow emission presented by Walker et al. 1988 (their Fig. 1; see also Mizuno et al. 1990; Ceccarelli et al. 1998; Hirano et al. 2001). As stated above, it has been proposed that the four lobes indicate the presence of two outflows: the brighter one along the east-west direction (east-blue and west-red lobes, hereafter EB and WR, respectively, in the nomenclature of Walker et al. 1988) and the other one along the northeast-southwest direction (northeast-red and southwest-blue lobes, hereafter

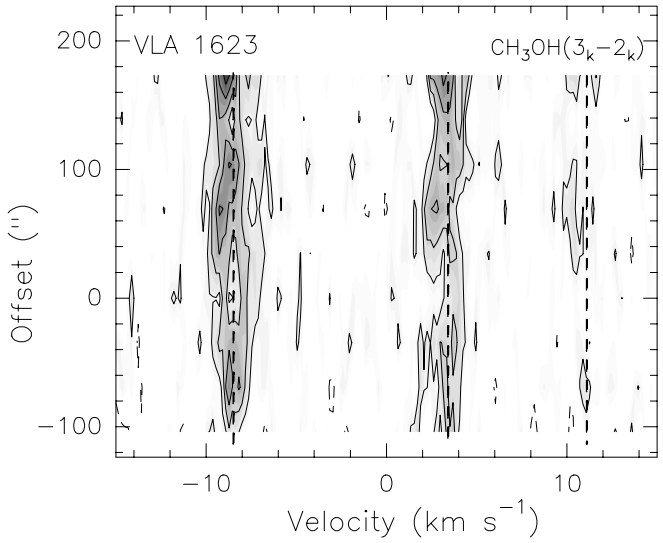

FIG. 9.—Position-velocity diagram of the CH_3OH ($3_k \rightarrow 2_k$) emission along the symmetry axis of the VLA 1623 outflow (P.A. 120°). Contour levels are drawn at −0.1 K and from 0.1 K up in steps of 0.1 K. The vertical dotted lines indicate the position of the different *k*-components for a systemic velocity of 3.4 km s^{-1}.

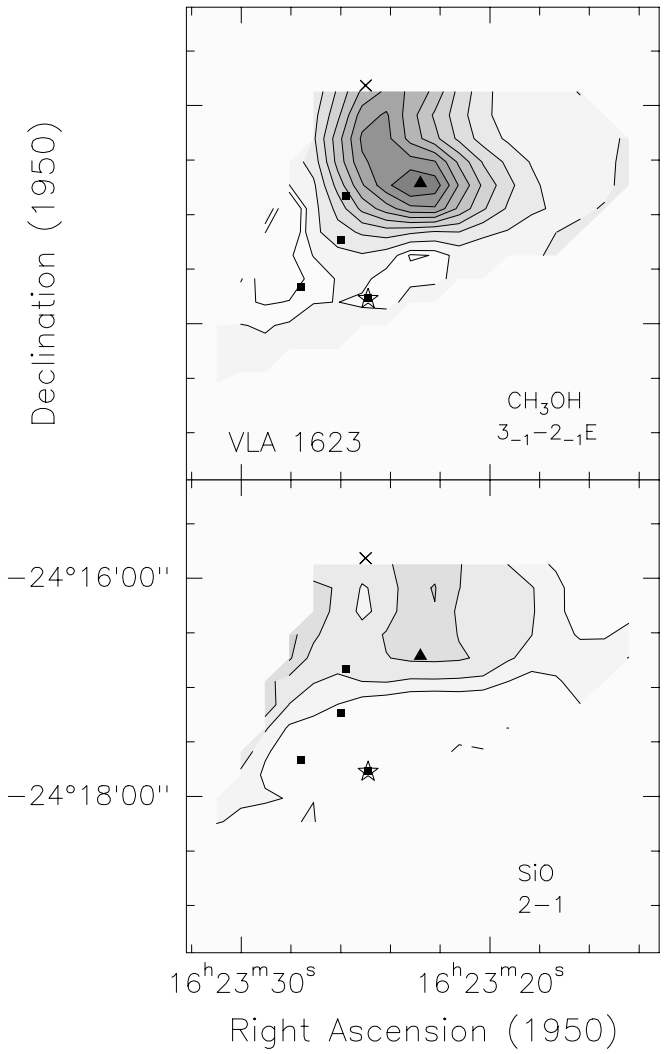

FIG. 10.—Contour maps of velocity-integrated emission from VLA 1623. The range of integration in v_{LSR} is from 1.8 to 5.2 km s^{-1}. The squares indicate the peak position of the four dust continuum sources detected at submillimeter wavelengths by André et al. (1993), one of which coincides with the radio source VLA 1623 (indicated by a star). The cross indicates the peak position of the ρ Oph A dense core (Loren & Wootten 1986). The position of the peak methanol emission, located at α(1950.0) = 16^{h}23^{m}22^s.8 and δ(1950.0) = −24°16′42″.7, is indicated by a triangle. *Top*: CH_3OH ($3_{-1} \rightarrow 2_{-1}$ *E*) emission. Contour levels are 5%, 10%, 20%, 30%, 40%, 50%, 60%, 70%, 80%, and 90% of the peak value of 2.8 K km s^{-1}. *Bottom*: SiO (2 → 1) emission. The lowest contour and contour interval are 0.065 K km s^{-1}.

NER and SWB, respectively). The peak positions of the different CO lobes are indicated by their names in the top panel of Figure 12.

The redshifted SiO and CH_3OH emissions detected northeast of IRAS 16293 lie within the NER CO lobe and have spatial extents similar to that of the CO emission. The peak of the SiO emission is coincident with the CO peak, whereas the peak in CH_3OH is shifted by ∼40″ in the direction of the central sources. The SiO line profiles show two shapes: at large distances from IRAS 16293 they exhibit a broad and flat redshifted feature, whereas at closer distances they show a peak near the ambient cloud velocity, a gradual decrease toward redshifted velocities, and a rapid decline toward blueshifted velocities. Hirano et al. (2001) and Castets et al. (2001) resolved the SiO emission in this direction into two components, labeled E1 and E2. Component E2 is seen in the velocity range from 2 to 20 km s^{-1} and its peak coincides with the CO peak of the NER lobe. Component E1 is seen in a narrower velocity range (2–10 km s^{-1}) and its peak is located 57″ east of IRAS 16293. Castests et al. (2001) argue that component E1 is not associated with the NER CO outflow lobe but marks the redshifted lobe from an outflow driven by the newly discovered object IRAS 16293E (Fig. 12). They suggest that this object powers an outflow that is responsible for the SiO emission at E1 (redshifted) and that has a corresponding blue lobe seen in H_2CO emission (their peak HE1, which is not covered by our maps).

The redshifted SiO and CH_3OH emissions observed northwest of IRAS 16293 lie projected toward the WR CO lobe; their intensities are considerably weaker than those seen toward the northeast. The SiO emission arises from a region of ∼30″ in radius, and its peak position is coincident with the WR CO peak. On the other hand, the methanol emission arises from a region that is closer to the northern boundary of the WR CO lobe, its peak being displaced ∼35″ northeast of the CO peak. The profiles of both the SiO and CH_3OH lines show a peak near the ambient cloud velocity, a gradual decrease toward redshifted velocities, and a rapid decline toward blueshifted velocities. The SiO emission in this direction was also resolved by Hirano et al. (2001) and Castets et al. (2001) into two components, labeled W1 and W2. Component W1 is coincident with the CO peak of the WR lobe.

The blueshifted SiO and CH_3OH emissions detected southeast of IRAS 16293 show significantly different spatial distributions. The SiO emission arises from a region elongated in the north-south direction, with a peak located ∼30″ west of the EB CO peak. The methanol wing emission arises from a more compact region located near the southern boundary of the EB CO lobe, with a peak located ∼70″ south of the EB CO peak. This blueshifted methanol structure is coincident with a strong blueshifted emission feature seen in formaldehyde (Castets et al. 2001; labeled

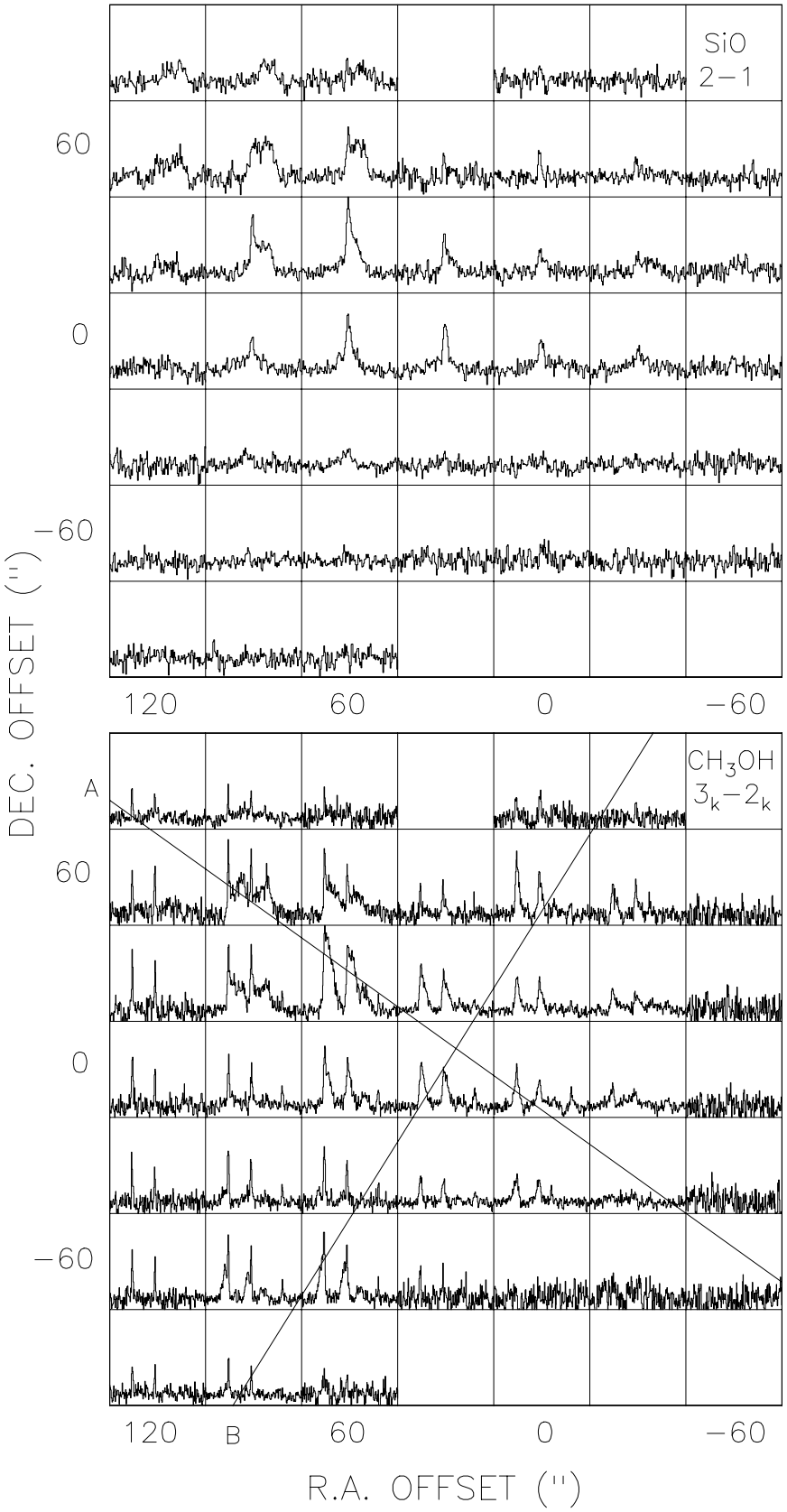

FIG. 11.—Observed spectra of the SiO ($2 \rightarrow 1$) (*top*) and CH_3OH ($3_k \rightarrow 2_k$) (*bottom*) line emission toward IRAS 16293−2422. The grid spacing is 30″. Offsets are from the reference position at $\alpha = 16^h29^m20^s.90$ and $\delta = -24°22'16''$ (B1950.0). In each box the velocity scale ranges from −20 to 30 km s^{-1}. The antenna temperature scale is from −0.2 to 1.7 K for CH_3OH and from −0.15 to 0.6 K for SiO.

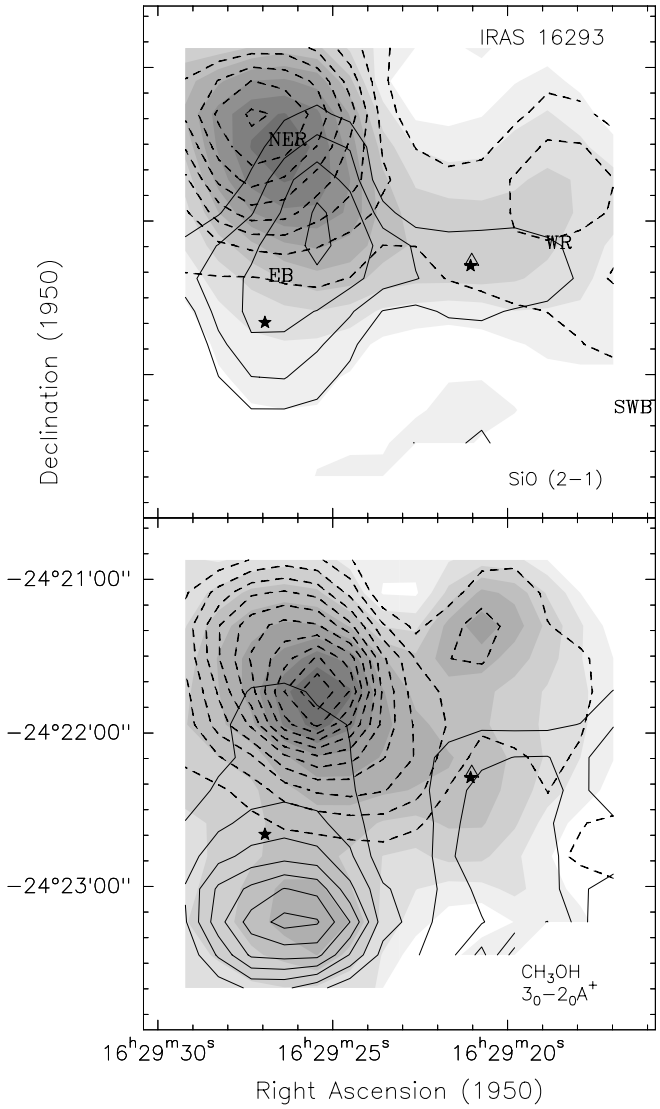

FIG. 12.—Contour maps of velocity integrated line wing emission from the IRAS 16293−2422 outflow. Continuous and dashed lines represent blueshifted and redshifted emission, respectively. The triangle marks the position of the radio continuum source VLA 16293−2422A and the stars the peaks of the 800 μm emission (Castets et al. 2001). *Top*: SiO ($2 \rightarrow 1$). Lowest contour and contour interval are 0.2 and 0.1 K km s^{-1} for the blueshifted emission ($v_{\rm flow}$: -6.4 to -1.1 km s^{-1}) and 0.3 K km s^{-1} for the redshifted emission ($v_{\rm flow}$: 2.9 to 14.3 km s^{-1}). The gray-scale map indicates the velocity-integrated emission. *Bottom*: CH_3OH (3_0–2_0 A^+). Lowest contour and contour interval are 0.2 K km s^{-1} for the blueshifted emission ($v_{\rm flow}$: -5.1 to -1.3 km s^{-1}) and 0.4 K km s^{-1} for the redshifted emission ($v_{\rm flow}$: 1.3 to 6.3 km s^{-1}). The gray-scale map indicates the methanol emission from *ambient gas* only (velocity-integrated emission from $v_{\rm LSR}$: 2.53 to 5.11 km s^{-1}).

HE2). The methanol line profiles toward this region show, in addition to a blueshifted component with a peak at a radial flow velocity of -1.8 km s^{-1} and a maximum radial flow velocity of -4.3 km s^{-1}, emission from a narrow ($\Delta v \sim 0.67$ km s^{-1}) component at the velocity of 3.76 km s^{-1}. The SiO line profiles show emission only from the blueshifted component. Finally, the blueshifted CH_3OH emission observed southwest of IRAS 16293 is associated with the SWB CO lobe, but its peak is displaced from the CO peak by $\sim 30''$ to the east. No SiO emission is detected toward the SWB lobe.

To investigate the kinematics of the SiO and CH_3OH emitting gas associated with the NER-SWB CO outflow, we show in Figure 13 a position-velocity diagram along a line with a P.A. of 55° (line A in Fig. 11), which corresponds to the major axis of the CO outflow. This diagram shows that the velocity of the SiO and CH_3OH emission from the NER lobe increases steadily with increasing distance from IRAS 16293. The largest line widths and higher velocities are found at the farthest distance from the central source. This velocity structure suggests that the emission in these molecules arises from a bow shock produced by a high-velocity jet impinging onto the ambient medium (see Masson & Chernin 1993). On the other hand, no outflow emission is detected in SiO or CH_3OH toward the SWB lobe. The question arises as to why the jet does not produce toward the southwest a lobe with similar characteristics to that in the northeast. We suggest that the absence of SiO and CH_3OH outflow emission toward the SWB CO lobe is due to a lack of available ambient material. We envision that in this direction the jet is moving in a low-density medium in a manner that is not entraining or sweeping up appreciable amounts of ambient gas. This hypothesis is supported by the spatial distribution of methanol emission in the range of velocities of the ambient cloud (see the gray-scale map in the bottom panel of Fig. 12), which shows an absence of emission southwest of the *IRAS* source, implying a lack of high-density gas in this direction. This may imply that the outflow is breaking out of the near side of the dense core, as

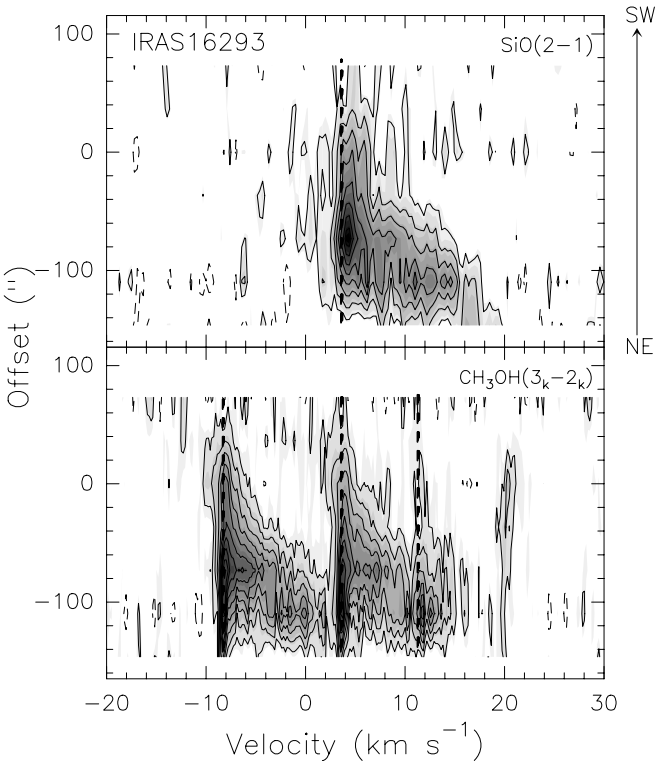

FIG. 13.—Position-velocity diagrams along the symmetry axis of the NER-SWB outflow from IRAS 16293 (P.A. 55°; line A in Fig. 11). *Top*: SiO ($2 \rightarrow 1$) emission. Contour levels are drawn at -0.06 K and from 0.06 K up in steps of 0.06 K. The vertical dotted line indicates the systemic velocity of the ambient gas of 3.64 km s^{-1}. *Bottom*: CH_3OH ($3_k \rightarrow 2_k$) emission. Contour levels are drawn at -0.15 K, and from 0.15 K up in steps of 0.15 K. The vertical dotted lines indicate the position of the different k-components for a systemic velocity of 3.64 km s^{-1}.

has been suggested by Castets et al. (2001), similar to the situation in BHR 71 (Bourke et al. 1997; Garay et al. 1998).

Figure 14 presents a position-velocity diagram along a line with a position angle of 145° joining the blueshifted southeast and redshifted northwest peaks of the CH_3OH wing emission (line B in Fig. 11). Note that this position angle differs significantly from that of the major axis of the EB-WR CO outflow. Castets et al. (2001) have suggested that in approximately this direction lies an outflow powered by IRAS 16293A + B. The *p-v* diagram shows that the velocity width of the methanol emission is approximately constant along the whole length of the emitting region, a result that may indicate that the outflowing gas is being driven by turbulent entrainment. It is possible that the methanol wing emission from the southeast and northwest regions arises from material entrained by a wide-angle stellar wind as it impinges into ambient medium clumps. This hypothesis is supported by the detection toward the CH_3OH outflow lobes of a strong and narrow component of methanol emission at the velocity of the ambient cloud (see bottom panel of Fig. 12). Further support comes from the H_2CO observations of Castets et al. (2001). The fact that these two molecules are detected, but not SiO, suggests that dust grain mantles are being destroyed, but not grain cores, which implies a less energetic process than direct interaction with a jet.

3.6. *Serpens S68N*

The S68N object corresponds to a molecular line peak in the northwest region of the Serpens star-forming core (McMullin et al. 1994; Williams & Myers 2000) at a distance of 310 pc (de Lara, Chavarría-K, & Lopez-Molina 1991). Associated with this core is the Class 0 source SMM 9 (Casali, Eiroa, & Duncan 1993; White, Casali, & Eiroa 1995; Hurt, Barsony, & Wootten 1996), which has a bolometric luminosity of 5.0 $L_\odot$ (Wolf-Chase et al. 1998). Outflow emission has been detected in a number of molecules toward this region (McMullin et al. 1994, 2000), although the data do not allow for a definitive assignment of the outflowing gas to particular protostellar sources (White et al. 1995; Davis et al. 1999). Interferometric observations in CS ($2 \rightarrow 1$) by Williams & Myers (2000) clearly show that S68N/SMM 9 is associated with a compact outflow oriented approximately northwest-southeast.

The observed spectra and maps of integrated emission in the SiO and CH_3OH lines have been presented elsewhere (Garay et al. 2002). Methanol and silicon monoxide wing emissions are detected at blueshifted velocities, with respect to the systemic ambient cloud velocity of 8.46 km s^{-1} (Hurt et al. 1996), toward the northwest region and at redshifted velocities toward the southeast, in agreement with the CS outflow (Williams & Myers 2000). The wing emission from the blue lobe extends up to a $v_{\rm flow}$ of -10.0 km s^{-1} in methanol and -9.4 km s^{-1} in silicon monoxide, whereas that from the red lobe extends up to a $v_{\rm flow}$ of 9.7 km s^{-1} in CH_3OH and 10.8 km s^{-1} in SiO. Figure 15 shows a position-velocity diagram along the symmetry axis of the

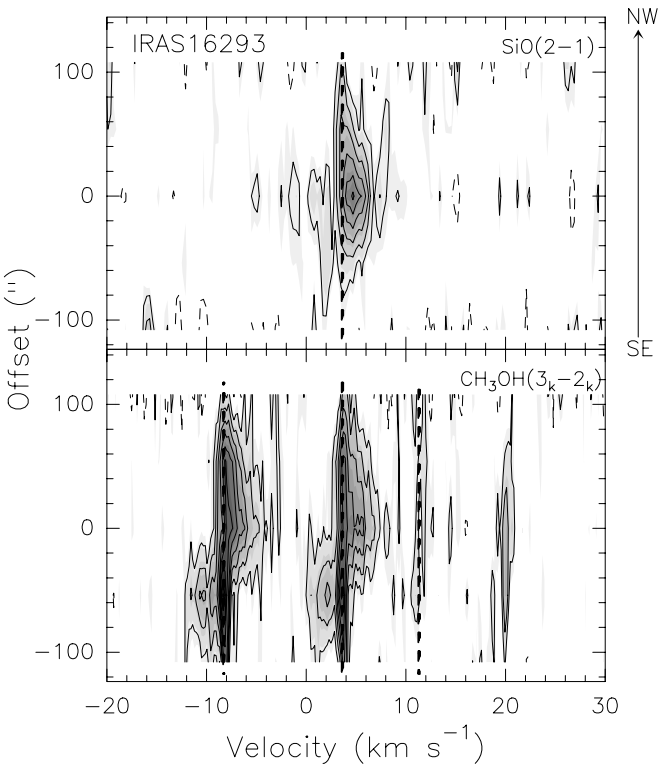

FIG. 14.—Position-velocity diagrams along a line joining the blueshifted southeast and redshifted northwest peaks of the CH_3OH wing emission from IRAS 16293 (P.A. 145°; line B in Fig. 11). *Top*: SiO ($2 \rightarrow 1$) emission. Contour levels are drawn at -0.06 K and from 0.06 K up in steps of 0.06 K. *Bottom*: CH_3OH ($3_k \rightarrow 2_k$) emission. Contour levels are drawn at -0.14 K and from 0.14 K up in steps of 0.14 K. Vertical dotted lines as in Fig. 13.

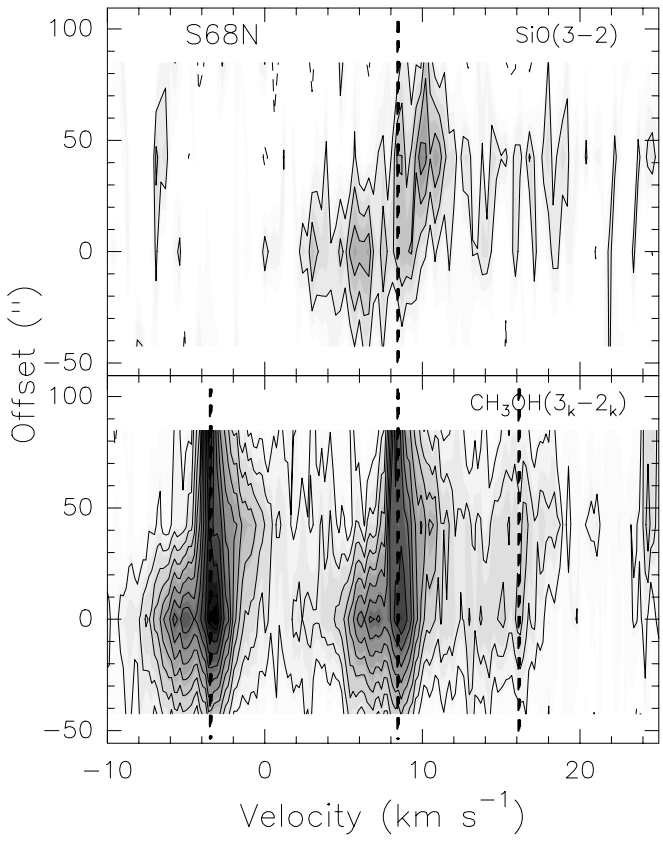

FIG. 15.—Position-velocity diagrams along the symmetry axis of the S68N outflow (P.A. 135°). *Top*: SiO ($3 \rightarrow 2$) emission. Contour levels are drawn at -0.06 K and from 0.06 K up in steps of 0.06 K. The vertical dotted line indicates the systemic velocity of the ambient gas of 8.46 km s^{-1}. *Bottom*: CH_3OH ($3_k \rightarrow 2_k$) emission. Contour levels are drawn at -0.12 K and from 0.12 K up in steps of 0.12 K. The vertical dotted lines indicate the position of the different *k*-components for a systemic velocity of 8.46 km s^{-1}.

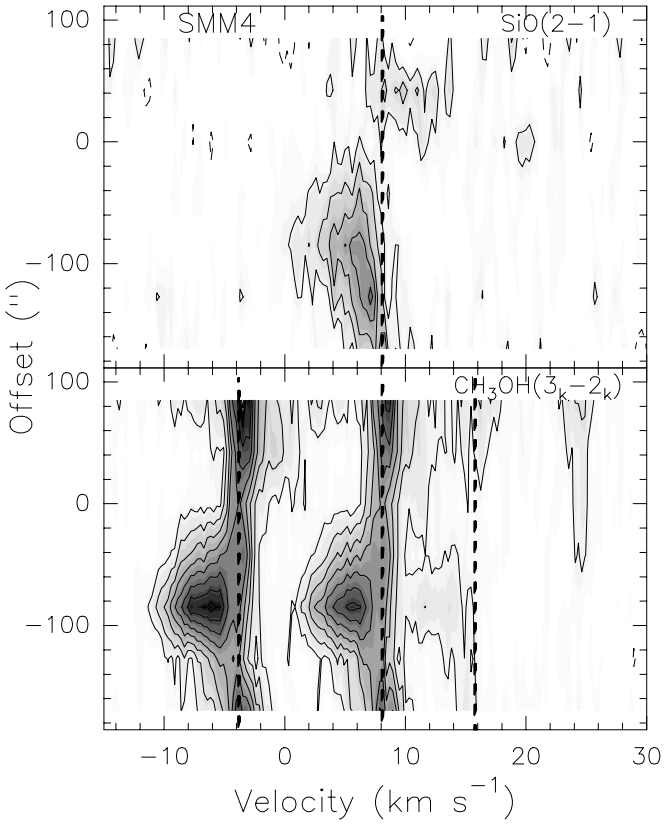

FIG. 16.—Position-velocity diagrams along the symmetry axis of the SMM 4 outflow (P.A. 135°). *Top*: SiO ($2 \rightarrow 1$) emission. Contour levels are drawn at -0.06 K and from 0.06 K up in steps of 0.06 K. The vertical dotted line indicates the systemic velocity of the ambient gas of 8.1 km s^{-1}. *Bottom*: CH_3OH ($3_k \rightarrow 2_k$) emission. Contour levels are drawn at -0.15 K and from 0.15 K up in steps of 0.15 K. The vertical dotted lines indicate the position of the different k-components for a systemic velocity of 8.1 km s^{-1}.

outflow (P.A. of 135°). This diagram suggests that the outflow emission arises from C-type bow shocks driven by a collimated jet (e.g., Masson & Chernin 1993), but observations with higher angular resolution are needed to assess this hypothesis.

3.7. *Serpens SMM 4*

The strongest millimeter continuum source in the southwest region of the Serpens star-forming cloud core is the Class 0 protostar SMM 4 (Casali et al. 1993), with a bolometric luminosity of 9 $L_\odot$ (Hurt & Barsony 1996). It is associated with bright molecular emission in several species (Hurt et al. 1996; Gregersen et al. 1997; McMullin et al. 2000), many of which show line profiles with blue asymmetry, characteristic of infall motions. White et al. (1995) detected high-velocity CO emission (presumably outflow) in several regions of the Serpens core, in particular near object SMM 4. However, because of the complex spatial structure of the high-velocity emission, it is difficult to associate the flows with individual sources.

The observed spectra and maps of integrated emission in the SiO ($2 \rightarrow 1$) and CH_3OH ($3_k \rightarrow 2_k$) lines have been presented elsewhere (Garay et al. 2002). Methanol and silicon monoxide wing emission are detected at redshifted velocities, with respect to the velocity of the quiescent ambient cloud of $\sim$8.1 km s^{-1} (Mardones et al. 1997), toward the southeast and at blueshifted velocities toward the northwest. The redshifted SiO wing emission is detected up to a $v_{\rm LSR}$ of $\sim$14.2 km s^{-1} ($v_{\rm flow} \sim 6.1$ km s^{-1}), while the blueshifted SiO wing emission is detected up to a $v_{\rm LSR}$ of ~ -1.2 km s^{-1} ($v_{\rm flow} \sim -9.3$ km s^{-1}). Figure 16 shows a position-velocity diagram along a P.A. of 45°. In both lobes the SiO and CH_3OH emission increases its velocity dispersion as the distance from the driving source increases. This spectral-spatial characteristic suggests that the outflow emission arises from C-type bow shocks generated by a high-velocity collimated velocity jet impinging onto the ambient medium (see Bence, Richer, & Padman 1996).

4. DISCUSSION

4.1. *Column Densities and Rotational Temperatures*

Column densities and temperatures were computed toward selected positions in the lobes of each outflow. The column density in the velocity range from v to $v + \Delta v$, N_v, and rotational temperature, $T_{\rm rot}$, of silicon monoxide and methanol were derived from a rotational diagram analysis (see, e.g., Linke, Frerking, & Thaddeus 1979; Blake et al. 1987), with the assumptions of optically thin conditions and local thermodynamical equilibrium, which relates the integrated line intensity, rotational temperature, and column density via

$$\frac{3k \int_v^{v+\Delta v} T_{\rm mb}\, dv}{8\pi^3 \mu^2 \nu S} = \frac{N_v}{Q(T_{\rm rot})} \exp\left(-\frac{E_u}{kT_{\rm rot}}\right), \qquad (1)$$

where μ, ν, and S are the transition dipole moment, frequency, and line strength of the transition, respectively, $\int_v^{v+\Delta v} T_{\rm mb}\, dv$ is the velocity-integrated main beam brightness, obtained directly from the observations, E_u is the upper-state energy, and $Q(T_{\rm rot})$ is the rotational partition function.

The column density of CO molecules in the velocity range from v to $v + \Delta v$, N_v(CO), was computed using the expression

$$N_v(\mathrm{CO}) = 2.31 \times 10^{14} \frac{T_{\rm ex} + 0.92}{1 - e^{-5.53/T_{\rm ex}}} \tau_v \Delta v \ \mathrm{cm}^{-2}, \qquad (2)$$

where $T_{\rm ex}$ is the excitation temperature of the outflowing gas and τ_v is the optical depth of the CO ($1 \rightarrow 0$) emission at outflow velocity v. The opacity was computed from the ratio of the observed emission in the ^{12}CO ($1 \rightarrow 0$) and ^{13}CO ($1 \rightarrow 0$) lines in the velocity range v, $v + \Delta v$, assuming an isotopic [^{12}CO/^{13}CO] abundance ratio of 67, corresponding to the average value in the solar neighborhood (Langer 1997), and excitation temperatures taken from the literature (see Bourke et al. 1997 for a description of the method). Because of the low strength of the ^{13}CO wing emission, in some cases this method did not permit to compute column densities in all ranges of flow velocities. Table 3 summarizes the total column densities and average rotational temperatures of the flowing gas in different outflow lobes.

4.2. *Chemical Enhancement*

The chemical composition of a gas cloud is usually characterized by the fractional abundance of molecules relative to molecular hydrogen, the main constituent of the interstellar gas. The abundance of H_2 in the outflow lobes is, however, not known and difficult to estimate. Therefore, in

TABLE 3

DERIVED PARAMETERS

SOURCE	LOBE	OFFSET (arcsec)	SILICON MONOXIDE v_{flow} (km s^{-1})	SILICON MONOXIDE N (cm^{-2})	METHANOL v_{flow} (km s^{-1})	METHANOL T_R (K)	METHANOL N (cm^{-2})
NGC 2264G.....	Blue	(−80, 20)	−6.5 → 0.5	1.3×10^{12}	−4.0 → 1.0	8.1 ± 1.0	2.6×10^{14}
IRAS 16293	NER	(90, 60)	0.0 → 14.0	7.3×10^{12}	0.0 → 8.0	8.6 ± 3.0	6.2×10^{15}
	NER	(60, 30)	0.0 → 10.0	6.2×10^{12}	0.0 → 8.0	7.8 ± 1.3	5.9×10^{15}
	EB	(90, −60)	−3.0 → −1.0	4.4×10^{11}	−4.0 → 0.0	10.8 ± 2.3	1.3×10^{15}
SMM 4	Blue	(60, −30)	−7.4 → 0.1	3.2×10^{12}	−4.8 → −0.3	8.3 ± 0.8	2.2×10^{15}
	Red	(30, −60)	1.6 → 5.6	1.7×10^{12}	0.3 → 4.8	8.2 ± 2.2	1.4×10^{15}
S68N	Blue	(−15, 0)	−4.2 → −0.2	1.2×10^{12}	−4.3 → −0.3	11.4 ± 4.0	1.2×10^{15}
	Red	(30, −45)	0.3 → 5.8	1.5×10^{12}	0.3 → 4.8	10.3 ± 3.2	1.2×10^{15}

the following discussion we will consider abundances relative to CO that can be directly derived from our observations. The fractional abundance of species X, [X/CO] (where X = SiO or CH_3OH), is computed as the ratio of the column density of species X, obtained from the rotational analysis, and the CO column density in the corresponding velocity range, obtained from the analysis of the CO and ^{13}CO lines.

To quantitatively assess the chemical changes of the ambient medium due to the outflow phenomena requires a knowledge of the chemical abundances of the quiescent ambient gas. However, the abundances of methanol and silicon monoxide in the ambient clouds harboring the collimated outflows studied here are not known. In dark clouds the [CH_3OH/CO] abundance ratio is 3×10^{-5} (Friberg et al. 1988; van Dishoeck et al. 1993), whereas for the [SiO/CO] abundance ratio only an upper limit of less than 3×10^{-8} exists (Ziurys, Friberg, & Irvine 1989; van Dishoeck et al. 1993). In the following we assume that the abundance ratios in the ambient gas surrounding the outflows are similar to those in dark clouds. Table 4 summarizes the peak fractional abundance and peak enhancement of SiO and CH_3OH in the different outflow lobes.

4.2.1. SiO *Enhancement*

Figure 17 shows the [SiO/CO] abundance ratio versus the absolute value of the radial flow velocity observed in the different outflow lobes. The peak [SiO/CO] abundance ratios are 1×10^{-5} in IRAS 16293 (red lobe) and SMM 4 (blue and red lobes), 5×10^{-6} in NGC 2264G (blue lobe), and 2.5×10^{-6} in S68N (blue lobe). The corresponding enhancements in the abundance of the gas-phase silicon monoxide in the outflow lobes, relative to quiescent ambient gas in dark globules, are 330, 170, and 80, respectively. The enhancement of SiO molecules in the lobes of molecular outflows is most likely due to the injection into the gas phase by shocks of Si atoms and/or Si-bearing species. Once silicon is injected into the gas phase, chemical models based on ion-molecule reactions predict a large abundance of SiO molecules (Turner & Dalgarno 1977; Hartquist, Oppenheimer, & Dalgarno 1980).

In the lobes of SMM 4 and S68N, the SiO abundance increases steeply with radial flow velocity, reaches a peak at a $|v_{flow}|$ of ∼3–4 km s^{-1}, and decreases gradually toward higher flow velocities. In the NER lobe of IRAS 16293 and blue lobe of NGC 2264G, the SiO abundance also increases steeply with radial flow velocity (up to a $|v_{flow}|$ of 5 km s^{-1}) and stays constant at higher flow velocities. The maximum radial outflow velocity of the SiO emission, v_{flow}^{max}(SiO), in the different outflow lobes ranges from 3.0 to 14.4 km s^{-1} (in absolute value). These moderate velocities, not fast enough to dissociate molecules, suggest that the production of SiO in the lobes is due to the presence of C-type shocks. In particular, the synthesis of molecules from atoms and ions can be highly efficient behind nondissociative C-type shocks. The main mechanism of injection of silicon is sputtering of Si-bearing material in grains driven by neutral particle impact on charged grains (Draine 1995; Flower &

TABLE 4

ABUNDANCE RATIOS AND ENHANCEMENTS

SOURCE	LOBE	OFFSET	ABUNDANCE RATIO [SiO/CO]	ABUNDANCE RATIO [CH_3OH/CO]	ENHANCEMENT SiO	ENHANCEMENT CH_3OH
NGC 2264G.....	Blue	(−80, 20)	5×10^{-6}	7×10^{-4}	170	23
IRAS 16293	NER	(90, 60)	1×10^{-5}	1.5×10^{-2}	330	500
	NER	(60, 30)	8×10^{-6}	1.0×10^{-2}	270	330
	EB	(90, −60)	9×10^{-7}	1.2×10^{-3}	30	40
SMM 4	Blue	(−60, 30)	3×10^{-6}	1.0×10^{-2}	100	330
	Red	(30, −60)	1×10^{-6}	1.2×10^{-3}	30	40
S68N	Blue	(−30, 0)	6×10^{-7}	2.4×10^{-3}	20	80
	Red	(30, −30)	5×10^{-7}	1.5×10^{-3}	20	50
Dark Clouds						
TMC-1	...	...	$< 3 \times 10^{-8}$	3×10^{-5}	1	1
L134N	...	...	$< 5 \times 10^{-8}$	4×10^{-5}	1	1

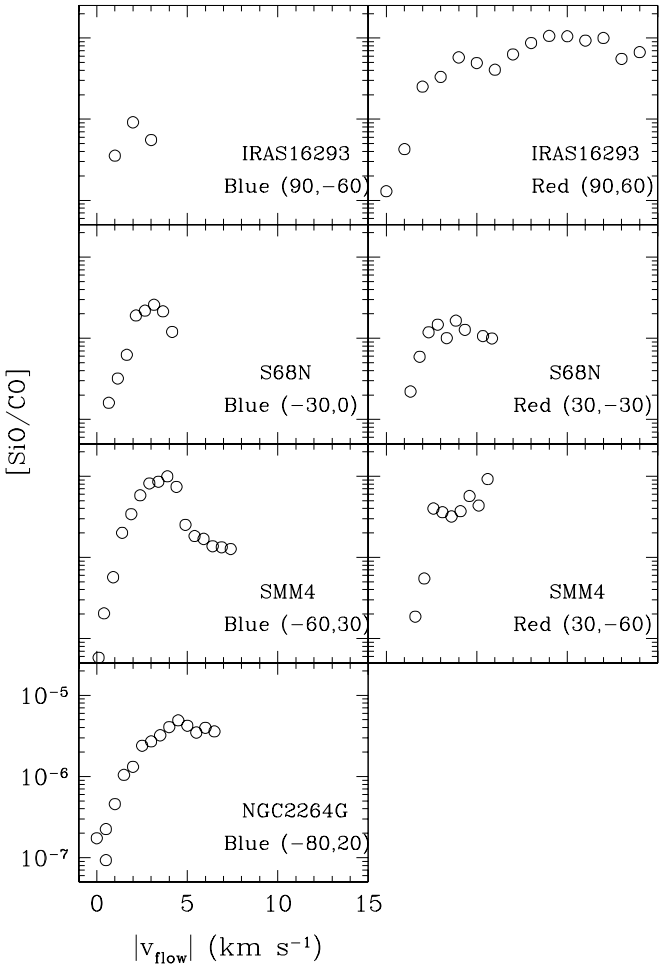

FIG. 17.—Abundance of SiO relative to CO vs. the absolute value of flow velocity observed in selected positions of different outflows. The object name and the position in the outflow are indicated in the lower right corner.

Pineau des Forêts 1995; Schilke et al. 1997), although grain-grain collisions become important for shocks propagating in dense regions [$n(H_2) > 5 \times 10^5$ cm^{-3}] at velocities ≥ 25 km s^{-1} (Caselli, Hartquist, & Havnes 1997). The sputtering of Si-bearing material can arise either from grain cores, namely, refractory grains that are composed of silicates and graphites, or from grain mantles (Schilke et al. 1997). In perpendicular C-type shocks, the release of Si-bearing material from grain cores requires higher impact energies than the release from mantles; substantial erosion of ice mantles can occur in C-shocks with velocities of ~ 25 km s^{-1}, while shock speeds of ~ 55 km s^{-1} are required in order to significantly erode the grain cores by He impacts. The inclusion of heavier species, such as CO and H_2O, can significantly lower the impact energies required for the erosion of grain cores, so that shock velocities as low as 25 km s^{-1} can cause substantial erosion of the grain cores (Schilke et al. 1997). The above constraints can be relaxed if oblique C-type shock models are used. In these models, the components of the relative velocities between grains and neutrals perpendicular to the shock propagation direction are comparable to or even larger than the component along it, resulting in efficient sputtering of volatile and refractory material by H_2 and He. Oblique C-type shocks with velocities between 30 and 35 km s^{-1} lead to gas-phase Si fractional abundances in the range 10^{-9}–10^{-6} (Caselli et al. 1997).

The total column densities of SiO at the peak position in the different outflow lobes range from 4.4×10^{11} to 7.3×10^{12} cm^{-2} (see Table 3). Codella, Bachiller, & Reipurth (1999) derived similar SiO column densities toward star-forming regions associated with molecular and Herbig-Haro outflows. Figure 18 shows the total column density of SiO versus the absolute value of the maximum SiO flow velocity observed in the different outflow lobes. Included in this figure are values derived for the NGC 2071 (Garay, Mardones, & Rodríguez 2000) and BHR 71 (Garay et al. 1998) outflows. There is a significant correlation between these two quantities, which suggests a velocity selective enhancement in the production of SiO molecules. Though the C-type shock models are still preliminary, most are able to explain column densities of SiO in molecular outflows within this range. The column densities predicted in the models of Schilke et al. (1997) are of the order of 10^{12} cm^{-2} at shock velocities of ~ 20 km s^{-1} and increase rapidly to $\sim 10^{15}$ cm^{-2} for a v_s of ~ 30 km s^{-1}. The observed (beam averaged) column densities suggest that in most of the sources the shock velocities are ≤ 20 km s^{-1}. For this moderate shock velocity, the silicon injected in the gas phase is mainly released from the ice mantle of the grains by heavy particle sputtering, the contribution from dust core sputtering being negligible.

Assuming that the maximum enhancement takes place at the critical velocity for grain mantle removal, which is about 10 km s^{-1} for a nonpolar and 20 km s^{-1} for a polar substrate (Schilke et al. 1997), it is possible to estimate the inclination angle of the outflow symmetry axis from the observed flow velocity at peak enhancement. In SMM 4 and S68N, the peak enhancement occurs at a radial flow velocity of ~ 3–4 km s^{-1}, implying inclination angles between 70° and 80°. In IRAS 16293 the *turnover* flow velocity is at ~ 7 km s^{-1}, implying an outflow inclination

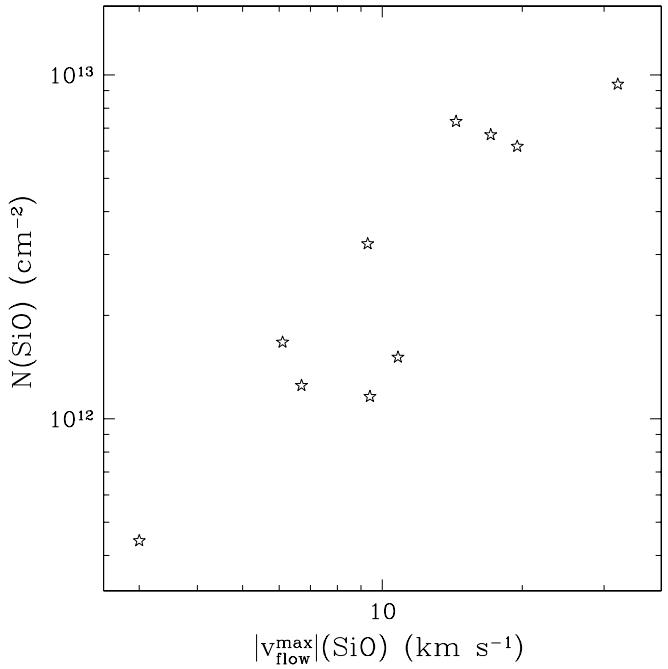

FIG. 18.—Relationship between column density of SiO and terminal SiO flow velocity of collimated bipolar outflows.

angle of $\sim 45°$. We notice, however, that this method can lead to highly uncertain values.

4.2.2. CH_3OH *Enhancement*

Figure 19 shows the [CH_3OH/CO] abundance ratio versus the absolute value of flow velocity observed in the different outflow lobes. The peak [CH_3OH/CO] abundance ratios are 1.5×10^{-2} in IRAS 16293 (red lobe), 1.0×10^{-2} in SMM 4 (blue lobe), 2.4×10^{-3} in S68N (blue lobe), and 7×10^{-4} in NGC 2264G (blue lobe). The corresponding enhancements in the gas-phase abundance of methanol in the outflow lobes, relative to quiescent ambient gas in dark globules, are 500, 330, 80, and 23, respectively. The large abundance of methanol, one of the most abundant ices on grain surfaces, is thought to arise from the evaporation of ice mantles (Tielens & Allamandola 1987; Charnley, Tielens, & Millar 1992; Bachiller et al. 1998; Blake et al. 1991) due to heating by low-velocity shocks, since volatile species, such as CH_3OH, HCN, and H_2CO, can survive sputtering or desorption of grain mantles only at low shock velocities ($v_s \leq 10$ km s^{-1}).

The column densities of CH_3OH at the peak position in the outflow lobes range from 2.6×10^{14} to 6.2×10^{15} cm^{-2} (see Table 3). Whether or not the C-type shock models described in the previous section are able to explain these column densities cannot be assessed since they have not considered the production of methanol. There is, however, a close correlation between the CH_3OH and SiO column densities derived toward the outflow lobes, suggesting a common origin of these two species. This is further supported by the similar dependences of the abundances of SiO and CH_3OH with flow velocity (see Figs. 17 and 19). We propose that in most of the outflows investigated here the SiO and CH_3OH trace the same excited gas, and attribute the production of these molecules to low-velocity shocks. The only exception is source NGC 2264G, for which the SiO to CH_3OH column density ratio is a factor of 4 times larger than average. The larger ratio may be attributed to an additional contribution to SiO by fast dissociative shocks. Models of the chemistry in regions behind fast dissociative shocks predict a substantial enhancement in the abundance of SiO molecules (Neufeld & Dalgarno 1989).

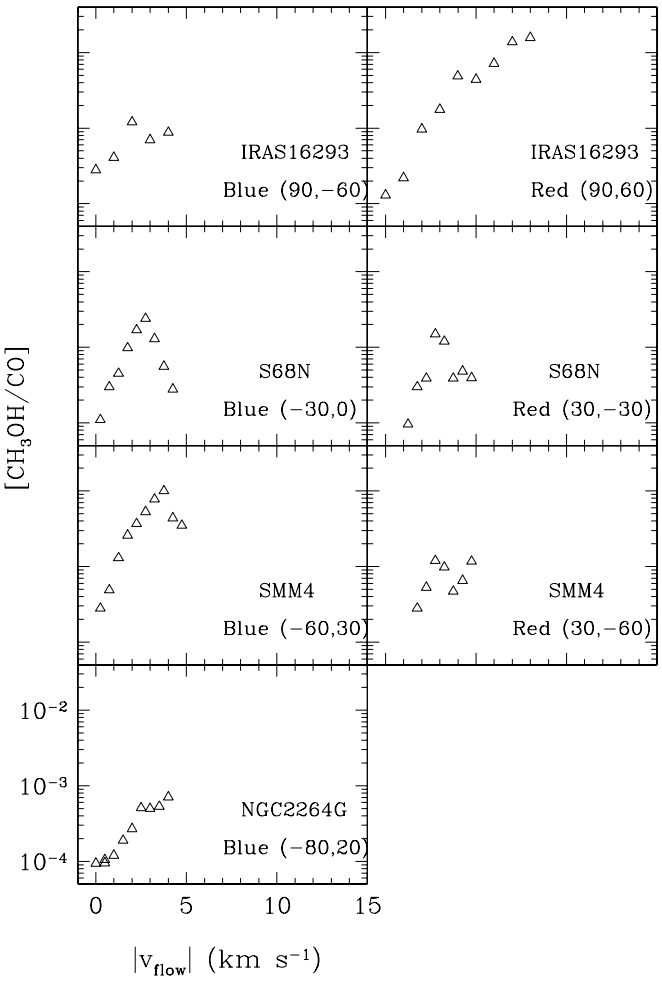

FIG. 19.—Abundance of CH_3OH relative to CO vs. the absolute value of flow velocity observed in selected positions of different outflows. The object name and the position in the outflow are indicated in the lower right corner.

We now turn the discussion to the CH_3OH abundance in the globules CG 30 and IRAS 13036, in which methanol emission is detected over extended regions (0.17 pc in CG 30 and 0.08 pc in IRAS 13036), but only at velocities close to the ambient cloud velocity. We find that the beam-averaged column densities of CH_3OH at the peak positions of CG 30 and IRAS 13036 are 2.9×10^{14} and 2.0×10^{14} cm^{-2}, respectively. The corresponding beam-averaged column densities of CO are 8.1×10^{17} and 3.0×10^{17} cm^{-2}, implying [CH_3OH/CO] abundance ratios of 3.6×10^{-4} and 6.7×10^{-4}. These values are roughly 10–20 times higher than those reported in quiescent cores and raise the question of the origin of the higher abundances. It has been argued that the driving source of the bipolar outflow in each of these two globules is in a more evolved stage of evolution than Class 0 objects. Chen et al. (1995) and Gregersen et al. (1997) suggest that CG 30 is on the boundary of the Class 0 category, whereas Lehtinen et al. (1999) argue that IRAS 13036 is a transitional object between Class 0 and Class I. It is possible that the enhancement of the CH_3OH abundance in these cores is still related to the outflow activity of their central sources, the lower enhancement compared with those of Class 0 objects being an indication of their later stages of evolution, at which the strength in outflow activity has considerably decayed.

The above discussion raises the question as to whether or not there is a correlation between abundance enhancement and age. We note beforehand that there are important issues that may prevent us from giving a definitive answer. First, there are large uncertainties in the age of the central sources. Most estimates correspond to the dynamical age of the outflowing gas ($t_D = R/v_{\rm flow}$); however, it is difficult to tie this age to the actual age of the protostar without knowing when the mass loss began and how the outflow propagates through the ambient medium. In addition, the enhancement is likely to depend also on the properties of the ambient medium in which the jet is impinging. This is clearly illustrated by the observed properties of the methanol emission from the different lobes of the NGC 2264G and IRAS 16293−2422 outflows (see §§ 3.1 and 3.5). The dependence of the enhancement with age and ambient medium may not be separable. Furthermore, differences in luminosities could also cause important differences on the evolution timescales. In spite of these caveats, we plot in Figure 20 the methanol enhancement observed in different outflow lobes versus the dynamical age of the outflow. Also

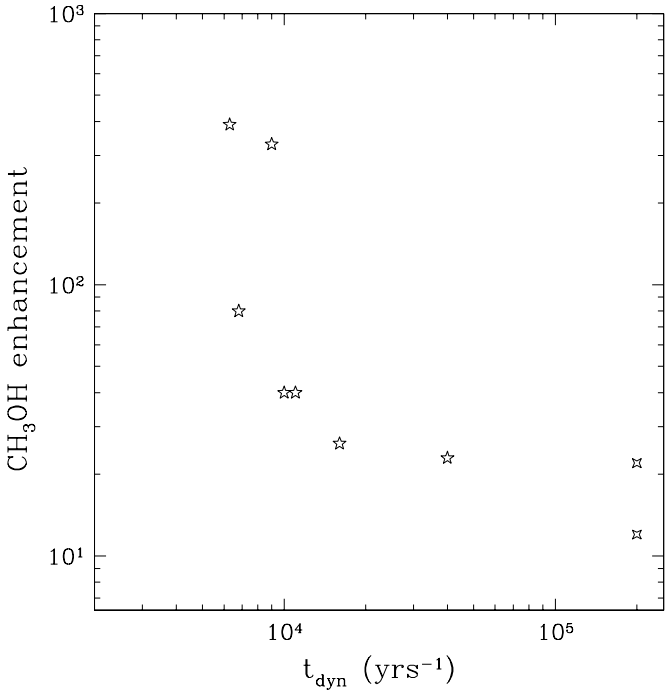

FIG. 20.—Relationship between methanol abundance enhancement and outflow dynamical age of collimated bipolar outflows.

plotted are the enhancements derived for globules CG 30 and IRAS 13036, for which we assigned a dynamical age of 2×10^5 yr, corresponding to the typical age of Class I sources (Wilking, Lada, & Young 1989). A glance to this figure may suggest that there is a decrease in abundance of methanol with age. This apparent relationship is, however, in disagreement with the null detection of methanol emission from the outflow lobes of VLA 1623. This object is considered to be the youngest Class 0 source, with a dynamical age of 2×10^3 yr (André et al. 1990), and hence the relationship predicts that the outflow lobes of VLA 1623 should show the strongest enhancement. It is worth mentioning here that the actual age of VLA 1623 may be considerably greater than its dynamical age. In fact, assuming that the continuum emission at submillimeter wavelengths arises from an accretion disk, Pudritz et al. (1996) estimated an age for the central energy source of 6×10^4 yr. We conclude that with the presently available data it is not possible to establish an age-enhancement relationship.

5. SUMMARY

We have mapped, using the SEST telescope, the silicon monoxide and methanol emission from seven collimated bipolar outflows thought to be associated with Class 0 objects: NGC 2264G, IRAS 08076−3556, IRAS 13036−7644, VLA 1623−243, IRAS 16293−2422, Serpens S68N, and Serpens SMM 4. The main results and conclusions presented in this paper are summarized as follows:

1. SiO and CH_3OH emission from outflowing gas were detected toward the lobes of four objects: NGC 2264G, IRAS 16293−2422, Serpens S68N, and Serpens SMM 4. The line profiles of the SiO emission from all these lobes, except IRAS 16293−2422, show a peak at a radial velocity close to but displaced from the ambient cloud velocity, and a gradual decrease in intensity from the peak toward higher flow velocities. This suggests that in these lobes a small fraction of the molecular gas is accelerated to shock velocities while the majority remains close to the ambient cloud velocity. This type of profile is characteristic of C-type bow shocks, where a range of shock speeds is present (Smith & Brand 1990).

2. The morphology of the SiO and CH_3OH wing emission from IRAS 16293−2422 shows a quadrupolar appearance, with the strongest redshifted emission arising from the NE region and the strongest blueshifted emission arising from the SE region. The velocity of the SiO and CH_3OH emission from the NER lobe increases steadily with increasing distance from IRAS 16293, reaching terminal outflow velocities of ~ 14 km s^{-1}. We propose that the emission in silicon monoxide and methanol from the NER lobe of IRAS 16293 arises from a bow-shock driven by a high-velocity collimated jet. No outflow emission is detected in SiO or CH_3OH toward the corresponding SWB lobe. We suggest that in this direction the collimated jet is interacting with a less dense medium than that toward the northeast and is moving in a manner that is not entraining or sweeping up appreciable amounts of ambient gas. The CH_3OH wing emission along the blueshifted southeast and redshifted northwest regions, which Castets et al. (2001) suggest is the place of an outflow powered by IRAS 16293A+B, shows a narrow and approximately constant velocity width along the whole length of the emitting region, a result suggestive of turbulent entrainment. The fact that emission is detected in methanol but not in silicon monoxide suggests that dust grain mantles are being destroyed but not grain cores, which implies a less energetic process than direct interaction with a jet. We suggest that the methanol wing emission from the southeast and northwest regions arises from material entrained by a wide-angle stellar wind as it impinges into ambient medium clumps.

3. The SiO abundance in the outflow lobes is enhanced with respect to that of quiescent ambient gas in dark globules by a factor of at least 330 in IRAS 16293−2422 and SMM 4, 170 in NGC 2264G, and 80 in S68N. The CH_3OH abundance is enhanced by a factor of 500 in IRAS 16293−2422, 330 in SMM 4, 80 in S68N, and 23 in NGC 2264G. In addition, we find that the dependence of the SiO/CO and CH_3OH/CO abundance ratios with radial flow velocity shows a steep increase in the range from ~ 0 to ~ 4–5 km s^{-1} and a gradual decline toward higher flow velocities. The large enhancements of methanol and silicon monoxide in the outflow lobes are most likely due to the release from grains of ice mantles and Si-bearing species via shocks produced by the interaction between the outflow and dense ambient gas.

4. The column densities of SiO at the peak position in the different outflow lobes range from 4.4×10^{11} to 7.3×10^{12} cm^{-2}. These column densities can be well explained by C-type shock models with moderate velocities (v_s: 10–20 km s^{-1}; Schilke et al. 1997). The column densities of CH_3OH at the peak position in the different outflow lobes range from 2.6×10^{14} to 6.2×10^{15} cm^{-2}. There is a close correlation between the CH_3OH and SiO column densities, suggesting a common origin of these two species.

In the remaining three sources (CG 30, IRAS 13036−7644, and VLA 1623−243), emission in methanol was detected from a narrow line at the velocity of the

ambient cloud, and no emission was detected in silicon monoxide. Weak methanol emission from a low-velocity outflow component was detected toward CG 30.

G. G. gratefully acknowledges support from a Cátedra Presidencial en Ciencias of the Chilean government and from the Chilean Fondecyt Projects 1980660 and 1010531. D. M. acknowledges support from the Chilean Fondecyt Project 1990632. P. C. acknowledges support from ASI (grants 98-116 and ARS-78-1999) and from MURST (project "Dust and Molecules in Astrophysical Environments").

REFERENCES

André, P., Martín-Pintado, J., Despois, D., & Montmerle, T. 1990, A&A, 236, 180
André, P., Ward-Thompson, D., & Barsony, M. 1993, ApJ, 406, 122
Bachiller, R. 1996, ARA&A, 34, 111
Bachiller, R., Codella, C., Colomer, F., Liechti, S., & Walmsley, C. M. 1998, A&A, 335, 266
Bachiller, R., & Pérez Gutiérrez, M. 1997, ApJ, 487, L93
Bachiller, R., Pérez Gutiérrez, M., Kumar, M. S. N., & Tafalla, M. 2001, A&A, 372, 899
Bachiller, R., & Tafalla, M. 1999, The Origin of Stars and Planetary Systems, ed. C. J. Lada & N. D. Kylafis (NATO ASI Ser. C, 540; Dordrecht: Kluwer), 227
Bence, S. J., Richer, J. S., & Padman, R. 1996, MNRAS, 279, 866
Blake, D., Allamandola, L., Sandford, S., Hudgings, D., & Freund, F. 1991, Science, 254, 548
Blake, G. A., Sandell, G., van Dishoeck, E. F., Groesbeck, T. D., Mundy, L. G., & Aspin, C. 1995, ApJ, 441, 689
Blake, G. A., Sutton, E. C., Masson, C. R., & Phillips, T. G. 1987, ApJ, 315, 621
Bourke, T. L., Garay, G., Lehtinen, K. K., Köhnenkamp, I., Launhardt, R., Nyman, L.-Å., May, J., Robinson, G., & Hyland, A. R. 1997, ApJ, 476, 781
Bourke, T. L., Hyland, A. R., & Robinson, G. 1995a, MNRAS, 276, 1052
Bourke, T. L., Hyland, A. R., Robinson, G., James, S. D., & Wright, C. M. 1995b, MNRAS, 276, 1067
Casali, M. M., Eiroa, C., & Duncan, W. D. 1993, A&A, 275, 195
Caselli, P., Hartquist, T. W., & Havnes, O. 1997, A&A, 322, 296
Castets, A., Ceccarelli, C., Loinard, L., Caux, E., & Lefloch, B. 2001, A&A, 375, 40
Ceccarelli, C., et al. 1998, A&A, 331, 372
Charnley, S. B., Tielens, A. G. G. M., & Millar, T. J. 1992, ApJ, 399, L71
Chen, H., Grenfell, T. G., Myers, P. C., & Hughes, J. D. 1997, ApJ, 478, 295
Chen, H., Myers, P. C., Ladd, E. F., & Wood, D. O. S. 1995, ApJ, 445, 377
Codella, C., Bachiller, R., & Reipurth, B. 1999, A&A, 343, 585
Davis, C. J., & Eislöffel, J. 1995, A&A, 300, 851
Davis, C. J., Matthews, H. E., Ray, T. P., Dent, W. R. F., & Richer, J. S. 1999, MNRAS, 309, 141
de Lara, E., Chavarría-K., C., & Lopez-Molina, G. 1991, A&A, 243, 139
Dent, W. R. F., Matthews, H. E., & Walther, D. M. 1995, MNRAS, 277, 193
Draine, B. T. 1995, Ap&SS, 233, 111
Draine, B. T., & McKee, C. F. 1993, ARA&A, 31, 373
Draine, B. T., Roberge, W. G., & Dalgarno, A. 1983, ApJ, 264, 485
Estalella, R., Anglada, G., Rodríguez, L. F., & Garay, G. 1991, ApJ, 371, 626
Fich, M., & Lada, C. J. 1997, ApJ, 484, L63
Flower, D. R., & Pineau des Forêts, G. 1995, MNRAS, 275, 1049
Friberg, P., Hjalmarson, A., Madden, S. C., & Irvine, W. M. 1988, A&A, 195, 281
Fukui, Y., Sugitoni, K., Takaba, H., Iwata, T., Mizuno, T., Ogawa, H., & Kawabata, K. 1986, ApJ, 311, L85
Garay, G., Köhnenkamp, I., Bourke, T. L., Rodríguez, L. F., & Lehtinen, K. K. 1998, ApJ, 509, 768
Garay, G., Mardones, D., & Rodríguez, L. F. 2000, ApJ, 545, 861
Garay, G., Mardones, D., Tafalla, M., Bachiller, R., & Myers, P. C. 2002, ApJ, submitted
Gredel, R. 1994, A&A, 292, 580
Gregersen, E. M., Evans II, N. J., Zhou, S., & Choi, M. 1997, ApJ, 484, 256
Gómez, J. F., Curiel, S., Torrelles, J. M., Rodríguez, L. F., Anglada, G., & Girart, J. M. 1994, ApJ, 436, 749
Hartley, M., Manchester, R. N., Smith, R. M., Tritton, S. B., & Goss, W. M. 1986, A&AS, 63, 27
Hartquist, T. W., Oppenheimer, M., & Dalgarno, A. 1980, ApJ, 236, 182
Henning, T., Wolf, S., Launhardt, R., & Waters, R. 2001, ApJ, 561, 871
Hirano, N., Mikami, H., Umemoto, T., Yamamoto, S., & Taniguchi, Y. 2001, ApJ, 547, 899
Hoddap, K.-W., & Ladd, E. F. 1995, ApJ, 453, 715
Hollenbach, D., & McKee, C. F. 1989, ApJ, 342, 306
Hughes, J., & Hartigan, P. 1992, AJ, 104, 680
Hurt, R. L., & Barsony, M. 1996, ApJ, 460, L45
Hurt, R. L., Barsony, M., & Wootten, A. 1996, ApJ, 456, 686
Lada, C. J., & Fich, M. 1996, ApJ, 459, 638
Langer, W. D. 1997, in IAU Symp. 170, CO: Twenty-Five Years of Millimeter-Wave Spectroscopy, ed. W. B. Latter et al. (Dordrecht: Kluwer), 98
Lehtinen, K. 1997, A&A, 317, L5
Lehtinen, K. 1998, The Physics and Chemistry of the Interstellar Medium (abstract book), ed. V. Ossenkopf (Aachen: Shaker), 106
Lehtinen, K., Lemke, D., & Mattila, K. 1999, The Universe as Seen by ISO, ed. P. Cox & M. F. Kessler (ESA SP-427; Noordwijk: ESA), 695
Leous, J. A., Feigelson, E. D., André, P., & Montmerle, T. 1991, ApJ, 379, 683
Linke, R. A., Frerking, M. A., & Thaddeus, P. 1979, ApJ, 234, L139
Loren, R. B., & Wootten, A. 1986, ApJ, 306, 142
Mardones, D., Myers, P. C., Tafalla, M., Wilner, D. J., Bachiller, R., & Garay, G. 1997, ApJ, 489, 719
Margulis, M., et al. 1990, ApJ, 352, 615
Margulis, M., & Lada, C. J. 1986, ApJ, 309, L87
Margulis, M., Lada, C. J., & Snell, R. L. 1988, ApJ, 333, 316
Masson, C. R., & Chernin, L. M. 1993, ApJ, 414, 230
McMullin, J. P., Mundy, L. G., Blake, G. A., Wilking, B. A., Mangum, J. G., & Latter, W. B. 2000, ApJ, 536, 845
McMullin, J. P., Mundy, L. G., Wilking, B. A., Hezel, T., & Blake, G. A. 1994, ApJ, 424, 222
Menten, K. M., Serabyn, E., Güsten, R., & Wilson, T. L. 1987, A&A, 177, L57
Mizuno, A., Fukui, Y., Iwata, T., Nozawa, S., & Takano, T. 1990, ApJ, 356, 184
Mundy, L. G., Blake, G. A., & Sargent, A. I. 1992, ApJ, 385, 306
Narayanan, G., Walker, C. K., & Buckley, H. D. 1998, ApJ, 496, 292
Neufeld, D. A., & Dalgarno, A. 1989, ApJ, 340, 869
Olberg, M., Reipurth, B., & Booth, R. S. 1989, in The Physics and Chemistry of Interstellar Molecular Clouds, ed. G. Winnewisser & J. T. Armstrong (Lecture Notes in Physics 331; Berlin: Springer), 120
Persi, P., Ferrari-Toniolo, M., Busso, M., Origlia, L., Robberto, M., Scaltriti, F., & Silvestro, G. 1990, AJ, 99, 303
Persi, P., Ferrari-Toniolo, M., Marenzi, A. R., Anglada, G., Chini, R., Krügel, E., & Sepúlveda, I. 1994, A&A, 282, 233
Pettersson, B. 1984, A&A, 139, 135
Pudritz, R. E., Wilson, C. D., Carlstrom, J. E., Oliver, P. L., Hills, R. E., & Ward-Thompson, D. 1996, ApJ, 470, L123
Raga, A. C., & Cabrit, S. 1993, A&A, 278, 267
Reipurth, B. 1981, A&AS, 44, 379
Richer, J. S., Shepherd, D. S., Cabrit, S., Bachiller, R., & Churchwell, E. 2000, in Protostars and Planets IV, ed. V. Mannings, A. P. Boss, & S. S. Russell (Tucson: Univ. Arizona Press), 867
Schilke, P., Walmsley, C. M., Pineau des Forêts, G., & Flower, D. R. 1997, A&A, 321, 293
Smith, M. D., & Brand, P. W. J. L. 1990, MNRAS, 245, 108
Tielens, A. G. G. M. 1999, in Formation and Evolution of Solids in Space, ed. J. M. Greenberg & A. Li (NATO ASI Ser. C, 523; Dordrecht: Kluwer), 331
Tielens, A. G. G. M., & Allamandola, L. J. 1987, in Physical Processes in Interstellar Clouds, ed. G. E. Morfill & M. Scholer (NATO ASI Ser. C, 210; Dordrecht: Reidel), 333
Tielens, A. G. G. M., McKee, C. F., Seab, C. G., & Hollenbach, D. J. 1994, ApJ, 431, 321
Turner, J. L., & Dalgarno, A. 1977, ApJ, 213, 386
van Dishoeck, E. F., & Blake, G. A. 1998, ARA&A, 36, 317
van Dishoeck, E. F., Blake, G. A., Draine, B. T., & Lunine, J. I. 1993, in Protostars and Planets III, ed. E. H. Levy & J. Lunine (Tucson: Univ. Arizona Press), 163
Walker, C. K., Carlstrom, J. E., & Bieging, J. H. 1993, ApJ, 402, 655
Walker, C. K., Lada, C. J., Young, E. T., Maloney, P. R., & Wilking, B. A. 1986, ApJ, 309, L47
Walker, C. K., Lada, C. J., Young, E. T., & Margulis, M. 1988, ApJ, 332, 335
Walker, M. F. 1956, ApJS, 2, 365
Ward-Thompson, D., Eiroa, C., & Casali, M. 1995, MNRAS, 273, L25
Westerlund, B. E. 1963, MNRAS, 127, 71
White, G., Casali, M. M., & Eiroa, C. 1995, A&A, 298, 594
Whittet, D. C. B., Assendorp, R., Prusti, T., Roth, M., & Wesselius, P. R. 1991, A&A, 251, 524
Wilking, B. A., & Lada, C. J. 1983, ApJ, 274, 698
Wilking, B. A., Lada, C. J., & Young, E. T. 1989, ApJ, 340, 823
Williams, J. P., & Myers, P. C. 2000, ApJ, 537, 891
Wolf-Chase, G. A., Barsony, M., Wootten, H. A., Ward-Thompson, D., Lowrance, P. J., Kastner, J. H., & McMullin, J. P. 1998, ApJ, 501, L193
Wootten, A. 1989, ApJ, 337, 858
Zhou, S. 1995, ApJ, 442, 685
Zinnecker, H., et al. 1999, A&A, 352, L73
Ziurys, L. M., Friberg, P., & Irvine, W. M. 1989, ApJ, 343, 201